DISCLAIMER

This report was prepared as an account of work sponsored by an agency of the United States Government. Neither the United States Government nor any agency thereof, nor any of their employees, makes any warranty, express or implied, or assumes any legal liability or responsibility for the accuracy, completeness, or usefulness of any information, apparatus, product, or process disclosed, or represents that its use would not infringe privately owned rights. Reference herein to any specific commercial product, process, or service by trade name, trademark, manufacturer, or otherwise does not necessarily constitute or imply its endorsement, recommendation, or favoring by the United States Government or any agency thereof. The views and opinions of authors expressed herein do not necessarily state or reflect those of the United States Government or any agency thereof. Reference herein to any social initiative (including but not limited to Diversity, Equity, and Inclusion (DEI); Community Benefits Plans (CBP); Justice 40; etc.) is made by the Author independent of any current requirement by the United States Government and does not constitute or imply endorsement, recommendation, or support by the United States Government or any agency thereof.

ANL/NSE-25/82

Improvement and Verification of Online Cross Section Generation Capability of Griffin for TRISO-fueled Reactors

Nuclear Science and Engineering Division

About Argonne National Laboratory
Argonne is a U.S. Department of Energy laboratory managed by UChicago Argonne, LLC under contract DE-AC02-06CH11357. The Laboratory's main facility is outside Chicago, at 9700 South Cass Avenue, Argonne, Illinois 60439. For information about Argonne and its pioneering science and technology programs, see www.anl.gov.

DOCUMENT AVAILABILITY

Online Access: U.S. Department of Energy (DOE) reports produced after 1991 and a growing number of pre-1991 documents are available free at OSTI.GOV (http://www.osti.gov/), a service of the US Dept. of Energy's Office of Scientific and Technical Information.

Reports not in digital format may be purchased by the public from the National Technical Information Service (NTIS):

U.S. Department of Commerce
National Technical Information Service
5301 Shawnee Rd
Alexandra, VA 22312
www.ntis.gov
Phone: (800) 553-NTIS (6847) or (703) 605-6000
Fax: (703) 605-6900
Email: **orders@ntis.gov**

Reports not in digital format are available to DOE and DOE contractors from the Office of Scientific and Technical Information (OSTI):

U.S. Department of Energy
Office of Scientific and Technical Information
P.O. Box 62
Oak Ridge, TN 37831-0062
www.osti.gov
Phone: (865) 576-8401
Fax: (865) 576-5728

Disclaimer
This report was prepared as an account of work sponsored by an agency of the United States Government. Neither the United States Government nor any agency thereof, nor UChicago Argonne, LLC, nor any of their employees or officers, makes any warranty, express or implied, or assumes any legal liability or responsibility for the accuracy, completeness, or usefulness of any information, apparatus, product, or process disclosed, or represents that its use would not infringe privately owned rights. Reference herein to any specific commercial product, process, or service by trade name, trademark, manufacturer, or otherwise, does not necessarily constitute or imply its endorsement, recommendation, or favoring by the United States Government or any agency thereof. The views and opinions of document authors expressed herein do not necessarily state or reflect those of the United States Government or any agency thereof, Argonne National Laboratory, or UChicago Argonne, LLC.

ANL/NSE-25/82

Improvement and Verification of Online Cross Section Generation Capability of Griffin for TRISO-fueled Reactors

---

Prepared by

Hansol Park and Changho Lee
Nuclear Science and Engineering Division, Argonne National Laboratory

September 30, 2025

Errata

After initial publication of this report the authors were made aware of some minor errors. These errors were corrected in the present version on **October 22, 2025**.

Location	Error	Correction
page iv	Missing acknowledgement for the use of INL HPC	Added
page 7	Wrong description of TRISO cell in Figure 2.1	$\mathsf{omm} + \mathsf{ir}$ instead of omm
page 8	Wrong upper equation in Eq. (2.1)	$(\Sigma_{\mathsf{mrt+ir},\mathrm{a}} + \Sigma_{\mathsf{mrt+ir},\mathrm{p}})$ instead of $\Sigma_{\mathsf{omm},\mathrm{t}}$

[This page left intentionally blank]

ABSTRACT

Griffin, a MOOSE-based reactor multiphysics code jointly developed by Idaho National Laboratory and Argonne National Laboratory under the DOE Office of Nuclear Energy's NEAMS program, has pursued the development of an online multigroup cross section generation capability for a few years to enable high-fidelity, problem-dependent neutronics analyses of advanced thermal reactors.

Recent advancements in Griffin's online multigroup cross section generation capability have significantly improved the accuracy, robustness, and efficiency of self-shielding calculations for both prismatic and pebble-bed TRISO-fueled reactor applications. Key developments include a unified fuel self-shielding method applicable to both TRISO and annular compact/spherical shell fuel zone geometries; an advanced Dancoff Category-based Equivalence Theory using a bell function for non-fuel resonance treatment, achieving more than an order-of-magnitude speedup compared to the Tone method; an on-the-fly multigroup equivalence approach to mitigate group condensation errors; and a streaming correction method for pebble-bed homogenization. A proof-of-concept demonstration of on-the-fly group condensation with consistent P_0 transport correction was also achieved. The method reproduced direct fine-group solutions with excellent accuracy (eigenvalue errors within 10 pcm and pin-power differences within 0.5%), but due to performance limitations of the current fixed-source solver, improvements to solver efficiency will be addressed in future work.

Verification tests were performed on graphite-moderated TRISO-fueled two-dimensional core benchmark problems representing gas-cooled microreactors, heat pipe-cooled microreactors, gas-cooled pebble-bed reactors, and fluoride salt-cooled high-temperature reactors. Across all cases, Griffin showed excellent agreement with Serpent2 continuous energy Monte Carlo solutions: eigenvalue errors within 200 pcm, pin-power root-mean-square errors within 2%, and control rod and drum worth errors less than 2%. It should be noted that, for the benchmark problem, cross section generation contributed less than 3% of the total simulation times.

These results demonstrate that Griffin's online cross section generation capability delivers accurate and efficient reactor physics solutions across a wide spectrum of TRISO-fueled advanced reactor designs. With further improvements to the fine-group fixed-source solver and planned extensions to depletion, transients, and coupled neutron–gamma transport, Griffin will be well-positioned to become a powerful and comprehensive tool for advanced reactor analysis.

ACKNOWLEDGEMENTS

This research was supported by the U.S. DOE under Contract number DE-AC02-06CH11357 for UChicago Argonne, LLC and supported by the DOE-NE Nuclear Energy Advanced Modeling and Simulation (NEAMS) program. This research made use of Idaho National Laboratory's High Performance Computing systems located at the Collaborative Computing Center and supported by the Office of Nuclear Energy of the U.S. Department of Energy and the Nuclear Science User Facilities under Contract No. DE-AC07-05ID14517. The authors are grateful to Ryan Willat for his valuable contributions to the verification tests of the online cross-section capability of Griffin for both pebble-type and prismatic-type reactor problems. They also thank Javier Ortensi and Rike Bostelmann for providing the original gPBR and gFHR benchmark problems.

Table of Contents

List of Figures

List of Tables

ACRONYMS

0D	zero-dimensional
1D	one-dimensional
2D	two-dimensional
3D	three-dimensional
BATSM	Bell function-based Analytic Two-region Slowing-down Method
CMFD	coarse-mesh finite difference
CMM	Cumulative migration method
CP	collision probability
CPM	collision probability method
DCET	Dancoff Category-based Equivalence Theory
DEM	discrete element method
DFEM	discontinuous finite element method
DoF	degrees of freedom
DSA	diffusion synthetic acceleration
EDC	Equivalence Dancoff factor Cell
ENCM	Enhanced Neutron Current Method
ESSM	Embedded Self-Shielding Method
FHR	fluoride high-temperature reactor
GCMR	Gas-Cooled Micro Reactor
GMRES	Generalized Minimal Residual method
HPMR	Heat Pipe-cooled Micro Reactor
HTGR	High-Temperature Gas-cooled Reactor
ILSS	Iterative Local Spatial Self-Shielding

IPSM	Improved Pin-based Slowing-down Method
IR	intermediate resonance
LWR	light water reactor
MOC	method of characteristics
NEAMS	Nuclear Energy Advanced Modeling and Simulation
NR	narrow resonance
PB-FHR	fluoride salt-cooled high temperature pebble-bed reactor
PBR	pebble-bed reactor
PDF	probability density function
PSM	Pin-based Slowing-down Method
RI	resonance integral
RMS	root mean square
SN	discrete ordinates
SPH	superhomogenization
SSAPI	Self-Shielding Application Programming Interface
TRISO	Tristructural Isotropic
XS	cross section

1. Introduction

Griffin [1, 2] is a MOOSE-based reactor multiphysics analysis code jointly developed by Argonne and Idaho National Laboratories under the DOE-NE Nuclear Energy Advanced Modeling and Simulation (NEAMS) program. A central goal of Griffin is to enable high-fidelity, problem-dependent neutronics simulations of advanced reactor systems, including prismatic block-type and pebble-bed-type high temperature reactors, molten-salt reactors, fast reactors, and micro-reactors.

A key component supporting this objective is the online multigroup cross section (XS) generation capability, provided through the Self-Shielding Application Programming Interface (SSAPI). The SSAPI produces region-wise multigroup XSs on the fly, explicitly accounting for heterogeneous fuel geometries, resonance effects, and streaming phenomena. Since its initial implementation [3], this capability has advanced substantially, with notable improvements in methodology, accuracy, and computational performance. To date, documentation of these developments has appeared only intermittently as subsections in previous reports, including the FY23 and FY24 milestone reports [4, 5]. This reports therefore provides the first comprehensive summary of the recent methodological advancements and associated verification results for two-dimensional (2D) core problems of advanced reactors of current interest.

Recent progress has focused on unifying and extending methodologies for both prismatic and pebble-bed reactor (PBR) applications. One major development is a unit cell-based slowing-down method with direct Dancoff correction to collision probability (CP) coefficients, applicable to both Tristructural Isotropic (TRISO) particle (micro-level) and compact or pebble (macro-level) self-shielding. The new method builds upon the Pin-based Slowing-down Method (PSM) approach [6] but extends it to TRISO problems with an improved application of the Dancoff correction to CP. This approach replaces the previous Iterative Local Spatial Self-Shielding (ILSS) method [7] for a TRISO-cell problem, achieving good speedup while maintaining comparable accuracy. It also serves as an alternative to the Equivalence Dancoff factor Cell (EDC) method previously used for compacts in prismatic gas-cooled reactors or pebbles in PBRs. Unlike the EDC method, the new approach eliminates the need for a binary search to determine the equivalent EDC size in a one-dimensional (1D) geometry and avoids the occasional convergence failures associated with that search. The methodology has further been extended to accommodate annular compacts and spherical-shell-type fuel zones in a pebble, enabling direct application to High-Temperature Gas-cooled Reactor (HTGR)s and fluoride salt-cooled high temperature pebble-bed reactor (PB-FHR)s without geometric approximations. This extension was achieved by deriving the TRISO Dancoff factor for such annular geometries.

For prismatic reactors, dedicated improvements have been made to treat non-fuel resonances more effectively. First, the existing Tone method based on heterogeneous XS tables [8] was extended to support homogeneous resonance integral (RI) tables. The homogeneous RI table was carefully generated to ensure homogeneous–heterogeneous equivalence within the Tone method for arbitrary geometries. Because the homogeneous RI table is not problem-specific, its generation procedure is included in the SSAPI library build, thereby eliminating the need to prepare heterogeneous tables for each target problem. Second, the Dancoff Category-based Equivalence Theory (DCET) method was developed as an alternative approach. Unlike the Tone method, which employs fixed-source calculations to numerically account for gray resonances, the developed method synthesizes the fuel escape probability by evaluating only the black limit and extending it to gray resonances using optical-thickness-dependent bell factors (bell functions) of an isolated black region that are obtained either analytically or numerically. In this approach, isotopes are grouped into Dancoff categories based on their black configurations, and a representative Dancoff factor is calculated for each category. Because a typical problem involves only a small number of unique black configurations, the number of fixed-source calculations is drastically reduced compared to that required by the Tone method. The uniqueness of this approach compared to the conventional Equivalence Theory method is the use of the bell function, eliminating the error caused by the N-term rational approximation and the need to perform fixed source calculations at several grey optical thickness points to derive the optimum N-term coefficients. Benchmarking confirmed that this approach achieves accuracy comparable to the Tone method while providing an order-of-magnitude speedup.

Additionally, an on-the-fly multigroup equivalence factor, historically referred to as superhomogenization (SPH) factor, has been introduced to mitigate condensation errors arising from neglecting the angular dependence of total XS in the resonance energy range [9]. Region-dependent factors within a fuel compact are obtained from unit cell-based on-the-fly slowing-down calculations and applied in the subsequent transport calculation. This correction is particularly important for cases with high TRISO packing fractions or strong moderator effects, where neglecting angular dependence tends to overestimate the neutron flux entering compacts and results in a negative reactivity bias of up to 300–400 pcm in strong cases.

For gas-cooled PBRs, a homogenization technique that accounts for pebble ensemble-wise flux weighting was first implemented in Griffin [10]. Building on this foundation, the SSAPI was further augmented with a streaming correction capability to capture the strong streaming effects arising from void regions between pebbles. In such environments, conventional flux-volume weighting underestimates the diffusion coefficient and, in turn, the leakage, leading to power tilts and an overestimation of eigenvalue. To address this streaming effect, the Benoist method [11] was applied to the existing pebble-bed collision probability method (CPM) solver developed in FY23 [10], providing a correction either to the diffusion coefficient for diffusion calculations or to the first-order self-scattering XS for transport calculations. In addition, accounting for region-dependent pebble volume fractions is important, as local variations influence resonance self-shielding and power distribution. To support this, a test script for evaluating pebble volume fractions cut by region boundaries in a 2D-RZ geometry in a very efficient manner has been verified and is planned to be merged into Griffin in the next FY.

Additionally, an on-the-fly energy group condensation scheme with consistent P0 transport correction has been introduced to improve performance. This approach reduces the number of groups used in multigroup transport relative to the fine-group library structure without resorting to equivalence parameters, thereby lowering computational costs while preserving accuracy. A proof-of-concept study has demonstrated promising results: condensed-group transport calculations reproduce fine-group solutions within 10–20 pcm in eigenvalue across a series of test problems and yield close power distributions within 0.5% difference.

In this report, Section 2 presents the theoretical background for the fuel and non-fuel self-shielding methods as well as the on-the-fly multigroup equivalence parameter. Section 3 describes the way to define local pebble-bed configurations and the homogenization technique with streaming correction for pebble-bed XS generation. Section 4 introduces the on-the-fly condensation scheme with consistent P_0 transport correction and provides preliminary verification results. Section 5 presents verification results for the gPBR (generic pebble-bed gas-cooled reactor) and gfluoride high-temperature reactor (FHR) (generic fluoride salt-cooled pebble-bed reactor) benchmark problems, along with the Gas-Cooled Micro Reactor (GCMR) and Heat Pipe-cooled Micro Reactor (HPMR) 2D core problems, focusing on both accuracy and performance. Finally, Section 6 concludes the report and outlines future work.

2. Improved Self-Shielding Method in SSAPI

This section outlines the self-shielding methodology in Griffin to evaluate self-shielded, fine-group microscopic XSs of all resonant isotopes in each heterogeneous region. The first subsection describes the self-shielding method for TRISO-bearing fuel, followed by the treatment of non-fuel resonances in the second subsection. Fuel resonances are handled using slowing-down calculations, whereas non-fuel resonances are treated either with the Tone method or with the newly developed DCET method using improved homogeneous RI tables. The specific efforts carried out in FY25 are highlighted in the relevant parts of this report.

2.1 Self-Shielding Method for TRISO-bearing Fuel

The ultrafine slowing-down method is employed as the self-shielding treatment for TRISO-bearing fuels. The basic idea is to obtain an ultrafine spectrum directly by performing slowing-down calculations in a unit cell and then use this spectrum as the weighting function to generate self-shielded XSs. The unit cell must properly capture the lattice shadowing effect, which is quantified by the Dancoff factor. The Dancoff factor is calculated prior to the slowing-down calculation and used to account for the shadowing effect in the unit-cell-based slowing-down procedure.

For regions containing TRISO, the self-shielding procedure consists of two stages: the first slowing-down calculation in a TRISO cell and the second slowing-down calculation in a macro cell. The first stage homogenizes XSs over the stochastic region (e.g., a compact or the fuel macro-region of a pebble) using flux-volume weighting at each ultrafine group in the slowing-down energy domain. The second stage condenses the stochastic-region-homogenized XSs into a fine-group structure. The resulting stochastic-region-averaged, self-shielded fine-group XSs are then used in subsequent flux calculations. If the fuel is a homogeneous fuel pellet without TRISO, only the second stage is required.

In terms of Dancoff-factor evaluation, only solid compacts and spherical fuel macro-regions of pebbles without non-fuel inner regions were supported prior to FY25. In FY25, the TRISO Dancoff factor evaluation capability was extended to include annular compacts for HTGRs and spherical-shell fuel macro-regions of pebbles for PB-FHRs. Regarding the slowing-down algorithms, the ILSS method [7] had been used for the first stage but was replaced by Bell function-based Analytic

Two-region Slowing-down Method (BATSM) [12] in FY24 [5]. For the second stage, the EDC method had been employed but was replaced in FY25 with the Improved Pin-based Slowing-down Method (IPSM) method. The designation "improved" refers to the enhanced treatment of the Dancoff correction, which is now applied to the CP coefficients in a manner consistent with Dancoff theory and applicable to arbitrary geometry types, in contrast to the original scheme [6].

This section provides not only the FY25 improvements but also the complete picture of the methodology of SSAPI. The first subsection gives an overview of the two-stage slowing-down calculation procedure. The second subsection describes the procedure for calculating Dancoff factors. The third subsection describes the improved methodology for incorporating the Dancoff factor into the slowing-down calculation.

2.1.1 Two-stage Slowing-down Procedure Overview

Fig. 2.1 illustrates the two-stage slowing-down procedure, which includes TRISO-cell and macro-cell problems and supports the presence of an inner region inside the TRISO-bearing macro-region. In the figure, the circle for the TRISO cell always represents a sphere, whereas that for the macro cell represents either a cylinder (with an inner region) for a prismatic-type reactor problem or a sphere (with an inner region) for a PBR problem.

The procedure begins with constructing the macro cell. In Step (A), a volume-homogenized mixture of any compositions outside the TRISO-bearing macro-region (typically a graphite block for a prismatic problem or the graphite shell of a pebble, coolant, and any dummy graphite pebbles for a PBR), labeled as `omm` in Fig. 2.1, is placed outside the TRISO-bearing macro-region, with the cell size determined by volume-ratio preservation. In Step (B), the probability of neutrons exiting the macro-region toward the outer region and subsequently reaching the macro region of another compact or pebble is calculated. This probability, denoted C^{mac}, represents the Dancoff correction factor for the macro cell (the complement of the Dancoff factor D). Its calculation method is explained in the next subsection.

Following Step (B), construction of the TRISO cell begins. In Step (C), a homogenized mixture of the inner region of the target macro-region and the `omm` region from the macro cell is placed outside the matrix region of a TRISO particle. In Step (D), the layers surrounding the fuel kernel, matrix, inner-region composition, and `omm` are volume-homogenized; this resulting mixture is la-

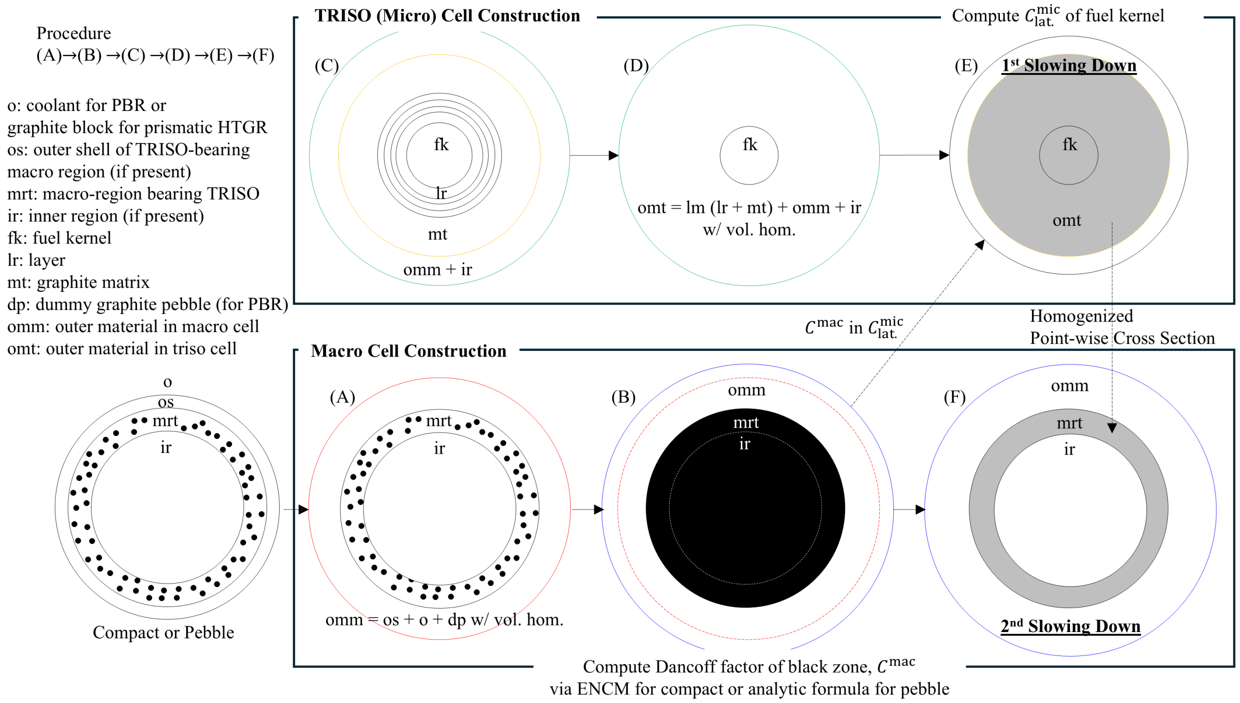

Figure 2.1. Two-stage slowing-down procedure of the self-shielding calculation for TRISO-bearing fuel.

beled `omt` in Fig. 2.1. In Step (E), $C^{\text{mic}}_{\text{lat.}}$ is calculated using the formula given in the next subsection, where the subscript "lat." indicates that inter-macro-region shadowing effects are considered.

The TRISO-cell slowing-down calculation is then performed using BATSM [12]. The method solves a two-region (fuel kernel + `omt`) slowing-down problem in which the CP coefficients at each ultrafine group are corrected by $C^{\text{mic}}_{\text{lat.}}$. The correction method is discussed later. Once the flux solution is obtained, the XSs of the TRISO cell (fuel kernel + TRISO layers + matrix) are averaged using flux-volume weighting at each ultrafine group. Note that the original volumes must be used in the weighting: $V_{\texttt{fk}}$ and $V_{\texttt{lm}}$, not $V_{\texttt{omt}}$ for the moderator.

The second slowing-down calculation is then performed in Step (F) using these averaged XSs. The IPSM method is used with the Dancoff factor $D^{\text{mac}} = 1 - C^{\text{mac}}$. Because C^{mac} accounts only for the region in the outer side of the fuel macro-region, interaction of the fuel macro-region with the inner region is treated locally through CP coefficients of the isolated combined region, and these coefficients are corrected together by D^{mac}. Once the spectrum for the fuel macro-region is obtained, it is used as the condensation weighting function to produce the final self-shielded XSs of the fuel macro-region.

For both slowing-down calculations, the same ultrafine groups with equal lethargy width of 1/2400 are used (about 60 ultrafine groups span the asymptotic scattering width of ^{238}U). A total of 24,840 ultrafine groups are used, covering the energy range from around 10 keV to 0.4 eV. Owing to the equal lethargy width, the scattering source can be updated recursively in a very efficient manner. To reduce computational cost, isotopes whose number density is less than 1% of the maximum in the composition are grouped into a single effective isotope whose mass is defined as the number-density-weighted average of all isotopes in the group.

2.1.2 Dancoff Factor Evaluation

As discussed above, two Dancoff factors are required: one for TRISO and one for the macro region. The macro-region Dancoff factor is calculated first because the TRISO Dancoff factor depends on it. For clarity, we discuss the Dancoff correction factor $C = 1 - D$ rather than D itself. The macro-region Dancoff correction factor is obtained using the Enhanced Neutron Current Method (ENCM) for prismatic-type problems or an analytic formula for pebble-bed reactors derived in Reference [13] (the dual-sphere method within an infinite pebble-bed region):

$$\begin{aligned} C^{\text{mac}} &= 1 - \bar{l}_{\mathsf{mrt+ir}}((\Sigma_{\mathsf{mrt+ir,a}} + \Sigma_{\mathsf{mrt+ir,p}})\phi_{\mathsf{mrt+ir}} - \Sigma_{\mathsf{mrt+ir,p}}) && \text{for prismatic type,} \\ C^{\text{mac}} &= \frac{e^{-2d^{\text{mac}}\Sigma_{\mathsf{omm,t}}}}{(\bar{l}_{\mathsf{omm}} - 2d^{\text{mac}})\Sigma_{\mathsf{omm,t}} + 1} && \text{for pebble type,} \end{aligned} \tag{2.1}$$

where subscripts t, a and p denote total, absorption and potential XSs, d^{mac} is the graphite-layer thickness of a pebble, and $\bar{l}$ denotes the average chord length. The quantities $\bar{l}_{\texttt{omm}}$ and $\bar{l}_{\texttt{mrt+ir}}$ are given by

$$\begin{aligned} \bar{l}_{\mathsf{mrt+ir}} &= \frac{4\,(V_{\mathsf{mrt}} + V_{\mathsf{ir}})}{S_{\mathsf{O,mrt}}}, \\ \bar{l}_{\mathsf{omm}} &= \frac{4\,V_{\mathsf{omm}}}{S_{\mathsf{O,mrt}}}, \end{aligned} \tag{2.2}$$

where $S_{\mathsf{O,mrt}}$ is the outer surface area of the fuel macro-region. The scalar flux ϕ in Eq. (2.1) for a prismatic type is obtained from the fixed-source problem formulated from ENCM:

$$\vec{\Omega}\cdot\vec{\nabla}\psi(\vec{r},\vec{\Omega})+\big(\Sigma_{\mathrm{a}}(\vec{r})+\Sigma_{\mathrm{p}}(\vec{r})\big)\psi(\vec{r},\vec{\Omega})=\frac{1}{4\pi}\Sigma_{\mathrm{p}}(\vec{r}),\qquad \begin{cases}\Sigma_{\mathrm{a}}(\vec{r})=10^5, & \text{for } \vec{r}\in\text{fuel region},\\ \Sigma_{\mathrm{a}}(\vec{r})=0, & \text{for } \vec{r}\in\text{non-fuel region}.\end{cases} \tag{2.3}$$

The inner region of the target macro-region is assumed to be black, consistent with the definition of C^{mac}. This C^{mac} is subsequently used in calculating the TRISO Dancoff correction factor $C^{\mathrm{mic}}_{\mathrm{lat.}}$, as explained below.

The inner region inside an annular macro-region is accounted for in the TRISO Dancoff correction factor. This consideration in $C^{\mathrm{mic}}_{\mathrm{lat.}}$ for the inner region was introduced in FY25. The discussion below is general enough that the formulas also apply to a solid macro-region without an inner region. The total correction is the sum of intra- and inter-pebble terms:

$$C^{\mathrm{mic}}_{\mathrm{lat.}}=C^{\mathrm{mic}}_{\mathrm{intra}}+C^{\mathrm{mic}}_{\mathrm{inter}}. \tag{2.4}$$

Fig. 2.2 depicts the CP coefficients used to calculate $C^{\mathrm{mic}}_{\mathrm{intra}}$ and $C^{\mathrm{mic}}_{\mathrm{inter}}$. Here, $C^{\mathrm{mic}}_{\mathrm{intra}}$ accounts for the probability that neutrons leaving a fuel kernel reach another fuel kernel without exiting the fuel macro-region ($C^{\mathrm{mic}}_{\mathrm{intra},\mathsf{mrt}}$), or exit to the inner side ($E^{*,\mathrm{d}}_{\mathrm{I}}$), re-enter the fuel macro-region (T_{ir}), and then reach another fuel kernel ($\gamma^{*,\mathrm{d}}_{\mathrm{I}}$) without collisions. The superscript $*$ denotes evaluation at the effective mean free path in the fuel macro-region, with inverse $\Sigma^*_{\mathsf{mrt}}=\Sigma_{\mathsf{lm},\mathrm{t}}+\frac{1}{\bar{l}_{\mathsf{lm}}-2d^{\mathrm{mic}}}$, where $\bar{l}_{\mathsf{lm}}=\frac{4r_{\mathsf{fk}}}{3}\left(\frac{1}{\mathrm{p.f.}\,(r_{\mathsf{fk}}/r_{\mathrm{TRISO}})^3}-1\right)$, p.f. denotes the TRISO packing fraction, and d^{mic} is the total width of the TRISO layers. The subscript lm refers to the homogenized mixture of TRISO layers outside the fuel kernel and the graphite matrix. The superscript d indicates the dual-sphere model, which accounts for the TRISO layers in the chord-length distribution between fuel kernels. Thus,

$$C^{\mathrm{mic}}_{\mathrm{intra}}=C^{\mathrm{mic}}_{\mathrm{intra},\mathsf{mrt}}+E^{*,\mathrm{d}}_{\mathrm{I}}T_{\mathsf{ir}}\gamma^{*,\mathrm{d}}_{\mathrm{I}}. \tag{2.5}$$

Meanwhile, $C^{\mathrm{mic}}_{\mathrm{inter}}$ accounts for neutrons exiting the fuel macro-region toward the outer side. It consists of four components: the escape probability from the fuel macro-region to the outer side (P_1), the transmission probability between different fuel macro-regions (P_2), the probability that neutrons entering from the outer side reach a fuel kernel (P_3), and the transmission probability

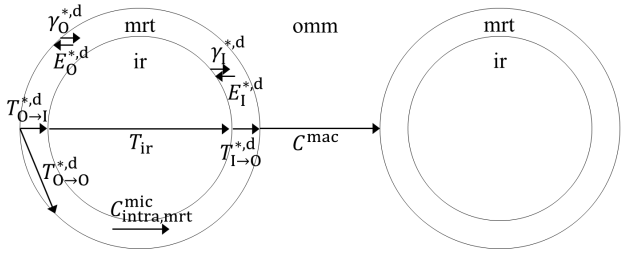

Figure 2.2. CP-coefficient diagram for annular-cylinder or spherical-shell geometry (I = inner surface, O = outer surface).

of the combined region comprising the fuel macro-region and the inner region (P_{t}). Allowing for multiple traversals of fuel macro-regions until a fuel kernel is reached [14],

$$C_{\mathrm{inter}}^{\mathrm{mic}} = P_1P_2P_3 + P_1P_2P_{\mathrm{t}}P_2P_3 + P_1P_2P_{\mathrm{t}}P_2P_{\mathrm{t}}P_2P_3 + \cdots = \frac{P_1P_2P_3}{1-P_{\mathrm{t}}P_2}, \tag{2.6}$$

where

$$P_1 = E_{\mathrm{O}}^{*,\mathrm{d}} + E_{\mathrm{I}}^{*,\mathrm{d}} T_{\mathsf{ir}} T_{\mathrm{I}\to\mathrm{O}}^{*,\mathrm{d}}, \tag{2.7}$$

$$P_2 = C^{\mathrm{mac}}, \tag{2.8}$$

$$P_3 = \gamma_{\mathrm{O}}^{*,\mathrm{d}} + T_{\mathrm{O}\to\mathrm{I}}^{*,\mathrm{d}} T_{\mathsf{ir}} \gamma_{\mathrm{I}}^{*,\mathrm{d}}, \tag{2.9}$$

and

$$P_{\mathrm{t}} = T_{\mathrm{O}\to\mathrm{O}}^{*,\mathrm{d}} + T_{\mathrm{O}\to\mathrm{I}}^{*,\mathrm{d}} T_{\mathsf{ir}} T_{\mathrm{I}\to\mathrm{O}}^{*,\mathrm{d}}. \tag{2.10}$$

The terms $C_{\mathrm{intra},\mathsf{mrt}}^{\mathrm{mic}}$, $E^{*,\mathrm{d}}$, $\gamma^{*,\mathrm{d}}$, and $T^{*,\mathrm{d}}$ are derived using the chord method. Following Reference [14], for surface $X \in \{\mathrm{O},\mathrm{I}\}$, they are

$$\begin{aligned}
C_{\mathrm{intra},\mathsf{mrt}}^{\mathrm{mic}} &= \frac{1}{\bar{l}_{\mathsf{mrt}}} \int dL \left(f_{\mathrm{O}}F_{\mathrm{O}}(L) + f_{\mathrm{I}}F_{\mathrm{I}}(L)\right) \int_{2d^{\mathrm{mic}}}^{L} dl \int_{2d^{\mathrm{mic}}}^{l} dl'\, f(l') e^{-\Sigma_{\mathsf{lm,t}} l'}, \\
E_{\mathrm{X}}^{*,\mathrm{d}} &= \frac{f_{\mathrm{X}}}{\bar{l}_{\mathsf{mrt}}} \int dL\, F_{\mathrm{X}}(L) \int_{2d^{\mathrm{mic}}}^{L} dl\, e^{-\Sigma_{\mathsf{lm,t}} l} \int_{l}^{\infty} dl'\, f(l'), \\
\gamma_{\mathrm{X}}^{*,\mathrm{d}} &= \int dL\, F_{\mathrm{X}}(L) \int_{2d^{\mathrm{mic}}}^{L} dl\, f(l) e^{-\Sigma_{\mathsf{lm,t}} l}, \\
T_{\mathrm{X}\to\mathrm{Y}}^{*,\mathrm{d}} &= \int dL\, F_{\mathrm{X}\to\mathrm{Y}}(L) e^{-\Sigma_{\mathsf{mrt}}^{*} L} \int_{L}^{\infty} dl\, f(l),
\end{aligned} \tag{2.11}$$

where f_{X} and $F_{\mathrm{X}}(L)$ denote the area fraction of surface X (out of the total inner-plus-outer area) and the probability density function (PDF) of chords starting from surface X, respectively. The average chord length of a spherical shell is $\bar{l}_{\mathsf{mrt}} = \frac{4V_{\mathsf{mrt}}}{S_{\mathrm{O}}+S_{\mathrm{I}}}$. The function $f(l)$ is the PDF of the chord length between fuel kernels within a fuel macro-region, approximated analytically in Reference [13] as

$$f(l) = \frac{1}{\bar{l}_{\mathsf{lm}} - 2d^{\mathrm{mic}}} \exp\left(-\frac{l - 2d^{\mathrm{mic}}}{\bar{l}_{\mathsf{lm}} - 2d^{\mathrm{mic}}}\right). \tag{2.12}$$

Using the transmission probabilities

$$\begin{aligned} \int dL\, F_{\mathrm{O}}(L)\, e^{-L\Sigma^*_{\mathsf{mrt}}} &= T^*_{\mathrm{O}\to\mathrm{O}} + T^*_{\mathrm{O}\to\mathrm{I}} \equiv T^*_{\mathrm{O}}, \\ \int dL\, F_{\mathrm{I}}(L)\, e^{-L\Sigma^*_{\mathsf{mrt}}} &= T^*_{\mathrm{I}\to\mathrm{O}} \equiv T^*_{\mathrm{I}}, \end{aligned} \tag{2.13}$$

and substituting Eqs. (2.12) and (2.13) into Eq. (2.11) yields

$$\begin{aligned} C^{\mathrm{mic}}_{\mathrm{intra},\mathsf{mrt}} &= C^{\mathrm{mic}}_{\infty,\mathsf{mrt}}\left(1 - \frac{2d^{\mathrm{mic}} + 1/\Sigma^*_{\mathsf{mrt}}}{\bar{l}_{\mathsf{mrt}}} + \frac{e^{2d^{\mathrm{mic}}\Sigma^*_{\mathsf{mrt}}}}{\Sigma^*_{\mathsf{mrt}}\bar{l}_{\mathsf{mrt}}}\left(f_{\mathrm{O}}T^*_{\mathrm{O}} + f_{\mathrm{I}}T^*_{\mathrm{I}}\right)\right), \\ E^{*,\mathrm{d}}_{\mathrm{X}} &= e^{-2d^{\mathrm{mic}}\Sigma_{\mathsf{lm},\mathrm{t}}}\, \frac{f_{\mathrm{X}}}{\bar{l}_{\mathsf{mrt}}\Sigma^*_{\mathsf{mrt}}}\left(1 - e^{2d^{\mathrm{mic}}\Sigma^*_{\mathsf{mrt}}}T^*_{\mathrm{X}}\right), \\ \gamma^{*,\mathrm{d}}_{\mathrm{X}} &= C^{\mathrm{mic}}_{\infty,\mathsf{mrt}}\, e^{2d^{\mathrm{mic}}\Sigma_{\mathsf{lm},\mathrm{t}}}\, \frac{\bar{l}_{\mathsf{mrt}}\Sigma^*_{\mathsf{mrt}}}{f_{\mathrm{X}}}\, E^{*,\mathrm{d}}_{\mathrm{X}}, \\ T^{*,\mathrm{d}}_{\mathrm{X}\to\mathrm{Y}} &= \exp\left(\frac{2d^{\mathrm{mic}}}{\bar{l}_{\mathsf{lm}} - 2d^{\mathrm{mic}}}\right) T^*_{\mathrm{X}\to\mathrm{Y}}, \end{aligned} \tag{2.14}$$

where the Dancoff factor of a fuel kernel in an infinitely large fuel macro-region is

$$C^{\mathrm{mic}}_{\infty,\mathsf{mrt}} = \frac{e^{-2d^{\mathrm{mic}}\Sigma_{\mathsf{lm},\mathrm{t}}}}{(\bar{l}_{\mathsf{lm}} - 2d^{\mathrm{mic}})\Sigma_{\mathsf{lm},\mathrm{t}} + 1}. \tag{2.15}$$

Analytic formulas for the three transmission probabilities in Eq. (2.13) can be found in Reference [15]. Note that a macro-region without an inner region is a special case of this formulation obtained by setting each quantity with subscript I in Eqs. (2.5), (2.7), (2.9) and (2.10) to zero.

2.1.3 Improved Dancoff Correction in Slowing-down Calculation

These Dancoff correction factors are used in the subsequent slowing-down calculations. At each ultrafine group, for a given scattering source into the group, the following CPM-based coupled equations for multiple fuel regions and one moderator region are solved:

$$\begin{aligned} V_i \Sigma_{i,\mathrm{t}} \phi_i &= \sum_j V_j F_j P^{\mathrm{lat}}_{j\to i} + V_\mathrm{m} F_\mathrm{m} P^{\mathrm{lat}}_{\mathrm{m}\to i}, \\ V_\mathrm{m} \Sigma_{\mathrm{m,t}} \phi_\mathrm{m} &= \sum_j V_j F_j P^{\mathrm{lat}}_{j\to \mathrm{m}} + V_\mathrm{m} F_\mathrm{m} P^{\mathrm{lat}}_{\mathrm{m}\to \mathrm{m}}, \end{aligned} \tag{2.16}$$

where subscripts i and j denote subregions in a fuel region, subscript m denotes the moderator region, F is the neutron source including self-scattering, and $P^{\mathrm{lat}}_{i\to j}$ is the first-flight collision probability from region i to region j in a lattice. A single moderator region (represented by a volume-homogenized composition of non-fuel regions in a unit cell, excluding the inner region for the macro-cell) is assumed, which is a good approximation for both TRISO and macro-cell problems.

The $P^{\mathrm{lat}}_{i\to j}$ are Dancoff-corrected CP coefficients that account for lattice shadowing. One widely used technique is the EDC method, previously used for the macro-cell slowing-down calculation in SSAPI but replaced here with the IPSM method. In the EDC method, the unit-cell size is adjusted so that the 1D-CPM Dancoff factor matches that from Eq. (2.1), and CP coefficients for the entire cell are obtained via numerical integration with the white boundary condition. Another approach is to correct the CP coefficients directly using the Dancoff factor [6]. This approach is faster than EDC (no equivalent-cell search, smaller integration domain) and more robust (the equivalent-cell search can fail to converge). SSAPI uses this idea in a two-region TRISO-cell problem for the first-stage calculation via the so-called bell function (BATSM, FY24). In FY25, an improved multi-region version replaced the previous EDC method for the macro-cell calculation. Conceptually the two techniques are identical; the difference is whether the problem is two-region (enabling direct use of the bell function) or multi-region (including non-fuel inner regions).

The Dancoff correction is traditionally derived for a two-region problem using the definition of the Dancoff factor, the probability that a neutron escaping the fuel surface undergoes its first collision in the moderator without passing through any other fuel region in the lattice:

$$P^{\mathrm{lat}}_{\mathrm{f}\to\mathrm{m}} = P^{\mathrm{iso}}_{\mathrm{esc,f}} D + \sum_{n=1}^{\infty} P^{\mathrm{iso}}_{\mathrm{esc,f}} (1-D)^n (1-\gamma^{\mathrm{iso}}_\mathrm{f})^n D, \tag{2.17}$$

where $P_{\mathrm{esc,f}}^{\mathrm{iso}}$ is the escape probability from an isolated fuel region and $\gamma_{\mathrm{f}}^{\mathrm{iso}} = \bar{l}_{\mathrm{f}}\Sigma_{\mathrm{f}}P_{\mathrm{esc,f}}$ is the first-flight blackness of the isolated fuel region ($\bar{l}_{\mathrm{f}}$ is the average chord length). The nth term represents the probability that, after escape, the first collision in the moderator occurs following n traversals of fuel.

To obtain a rational form suitable for heterogeneous–homogeneous equivalence, $P_{\mathrm{esc},f}^{\mathrm{iso}}$ has traditionally been approximated by a one-term rational expression with a single bell factor a_{B},

$$P_{\mathrm{esc},f}^{\mathrm{iso}} \approx \frac{a_{\mathrm{B}}}{\bar{l}_{\mathrm{f}}\Sigma_{\mathrm{f}} + a_{\mathrm{B}}},$$

followed by Dancoff correction, or by two-/three-term rational forms with (generalized) Stamm'ler's correction. A more recent approach employs an N-term rational fit to numerically computed $P_{\mathrm{f}\to\mathrm{m}}^{\mathrm{lat}}$ at selected optical thicknesses via fixed-source calculations [16, 17].

In SSAPI, this complication is avoided by casting $P_{\mathrm{esc},f}^{\mathrm{iso}}$ directly into a one-term rational form using pre-tabulated, optical-thickness-dependent bell factors $a_{\mathrm{B}}(\tau)$,

$$\frac{a_{\mathrm{B}}(\tau)}{\tau + a_{\mathrm{B}}(\tau)}, \quad \tau = \bar{l}_{\mathrm{f}}\Sigma_{\mathrm{f}},$$

with tables hardwired for cylindrical, spherical, and slab geometries. Fewer than 25 tabulated points achieve 0.1% accuracy per geometry type as shown in Fig. 2.3. Consequently,

$$P_{\mathrm{esc},f}^{\mathrm{lat}} = \frac{g(\tau)}{\tau + g(\tau)}, \qquad g(\tau) = \frac{a_{\mathrm{B}}(\tau)D}{a_{\mathrm{B}}(\tau)(1-D)+D}, \tag{2.18}$$

is an exact expression (due to tabulated $a_{\mathrm{B}}(\tau)$), and $P_{\mathrm{f}\to\mathrm{m}}^{\mathrm{lat}}$ follows immediately.

This approach is used in BATSM for the TRISO-cell problem, where at each ultrafine group $P_{\mathrm{f}\to\mathrm{m}}^{\mathrm{lat}}$ is evaluated via Eq. (2.18) and the two-region version of Eq. (2.16) is solved for flux. [5, 12] The same idea is also used in the newly developed DCET method for non-fuel resonance treatment, which is discussed in a later section.

For macro-region problems (e.g., a compact or pebble fuel macro-region), where resonance scattering significantly affects the source distribution, the logic of Eq. (2.17) extends to multiple fuel regions. The Dancoff-corrected fuel-to-fuel collision probability is

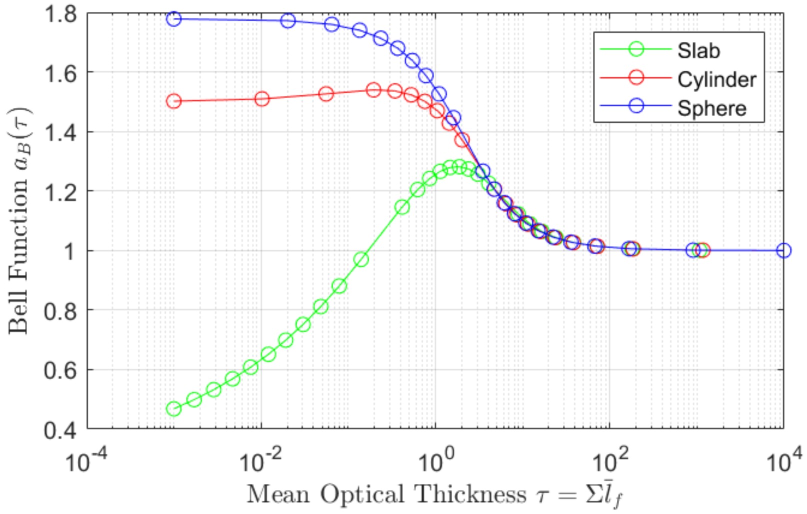

Figure 2.3. Bell factor as a function of the mean optical thickness for infinite slab, cylinder, and sphere geometries.

$$\begin{aligned} P^{\text{lat}}_{i\to j} &= P^{\text{iso}}_{i\to j} + \sum_{n=0}^{\infty} P^{\text{iso}}_{\text{esc},i}(1-D)^n(1-\gamma^{\text{iso}}_{\text{f}})^n(1-D)\gamma^{\text{iso}}_j \\ &= P^{\text{iso}}_{i\to j} + P^{\text{iso}}_{\text{esc},i}\,\frac{1-D}{1-(1-D)(1-\gamma^{\text{iso}}_{\text{f}})}\,\gamma^{\text{iso}}_j, \end{aligned} \tag{2.19}$$

where γ^{iso}_j is the first-flight blackness of subregion j. Since $P^{\text{iso}}_{i\to j}$ and γ^{iso}_j for all j, as well as $\gamma^{\text{iso}}_{\text{f}} = \sum_i \gamma^{\text{iso}}_i$, are readily obtained from one-dimensional numerical integration, $P^{\text{lat}}_{i\to j}$ is straightforward to evaluate. Once fuel-to-fuel CPs are determined, the remaining CPs involving the moderator follow from conservation and reciprocity:

$$\begin{aligned} P^{\text{lat}}_{i\to \text{m}} &= 1 - \sum_{j\in \text{f}} P^{\text{lat}}_{i\to j}, \\ P^{\text{lat}}_{\text{m}\to i} &= \frac{V_i\Sigma_i}{V_{\text{m}}\Sigma_{\text{m}}}\,P^{\text{lat}}_{i\to \text{m}}, \\ P^{\text{lat}}_{\text{m}\to \text{m}} &= 1 - \sum_{j\in \text{f}} P^{\text{lat}}_{\text{m}\to j}. \end{aligned} \tag{2.20}$$

Note that the non-fuel inner region inside the fuel macro-region is included in the indices i and j. That is, isolated-condition CPs are computed by numerical integration in all regions inside the outer surface of the fuel macro-region. These Dancoff-corrected CP coefficients are precomputed at several total XS values of the fuel macro-region for each pin prior to the slowing-down calculation and interpolated at the target XS during the calculation.

The correction method in Eq. (2.19) is fully consistent with Dancoff theory and applicable to arbitrary geometries, whereas the original PSM correction was less rigorous and derived only for cylindrical geometry. A further practical issue concerns the moderator volume V_m in Eq. (2.16). The choice of V_m is not explicit in Reference [6]. For light-water reactor lattices, where the pin unit cell is well defined, this ambiguity may be negligible. For advanced designs with irregular pin arrangements or supercells (fuel, heat pipes, moderator pins), the definition is less obvious. Using only the moderator volume of a fuel pin cell can overestimate the moderator source into fuel (see Eq. (2.20)), leading to stronger resonance absorption and a lower eigenvalue. Numerical tests confirm that using the moderator volume of an equivalent Dancoff-factor cell yields results nearly identical to the EDC method; however, deriving such a cell defeats the purpose of the IPSM. In practice, the results are not highly sensitive to V_m, and a reasonable approximation suffices. A suitable estimate follows from a Dancoff-factor expression based on the exponential chord-length distribution [18]:

$$D = \frac{1}{\dfrac{4V_\mathrm{m}}{S_\mathrm{f}}\Sigma_\mathrm{m} + 1} \quad \Rightarrow \quad V_\mathrm{m} = \frac{S_\mathrm{f}(1-D)}{4\Sigma_\mathrm{m} D}. \tag{2.21}$$

Once the lattice CP coefficients are obtained, the coupled linear system Eq. (2.16) is solved using a direct LU decomposition, where the left-hand-side matrix is defined as $A_{ij} = V_i \Sigma_{\mathrm{t},i}\delta_{ij} - V_j P_{j\to i}\Sigma_{\mathrm{s},j}$ and the right-hand-side vector is defined as $b_i = \sum_j V_j P_{j\to i} Q_j$ where Q_j is down-scattering source in region j.

2.1.4 Multigroup Equivalence

Evaluating self-shielded XSs is not the end of the story. It has long been recognized that directly using self-shielded XSs in heterogeneous transport calculations does not preserve reaction rates [19]. The detailed reason, however, was not identified until Reference [9], which showed that the root cause is the neglect of the angular dependence of resonance multigroup XSs.

Near strong resonances of ^{238}U, the spectrum of neutrons entering the fuel region is much less shielded than that of neutrons leaving it. Consequently, the multigroup XS seen by incoming neutrons is significantly larger than that seen by outgoing neutrons. If only scalar flux spectrum–weighted XSs are used, neutrons effectively enter the fuel too easily and escape less readily, leading to an overpopulation of neutrons in the fuel, enhanced resonance absorption, and a negatively biased eigenvalue. The study [9] showed that the effect is approximately -200 to -300 pcm regardless of energy group structure for light water reactor (LWR) problems. For this reason, a multigroup equivalence parameter is required. This parameter has traditionally been called the SPH factor, by analogy with homogenization error, even though it has no direct relation to homogenization.

To generate the SPH factor, a higher-order solution is needed. Fortunately, SSAPI already provides such information from ultrafine slowing-down calculations. The basic procedure follows the approach of [19]. From the ultrafine slowing-down solution, reference fine-group fluxes, sources, and total XSs for each region i in a fuel pin are obtained as

$$\phi^{\mathrm{ref}}_{g,i} = \sum_{\mathrm{ufg}\in g} \phi^{\mathrm{ref}}_{\mathrm{ufg},i}, \quad Q^{\mathrm{ref}}_{g,i} = \sum_{\mathrm{ufg}\in g} \left(q^{\mathrm{ref}}_{\mathrm{ufg},i} + \Sigma_{\mathrm{s,ufg}\to\mathrm{ufg},i}\phi^{\mathrm{ref}}_{\mathrm{ufg},i} \right), \quad \Sigma^{\mathrm{ref}}_{\mathrm{t},g,i} = \frac{\sum_{\mathrm{ufg}\in g} \Sigma_{\mathrm{t,ufg},i}\phi^{\mathrm{ref}}_{\mathrm{ufg},i}}{\sum_{\mathrm{ufg}\in g} \phi^{\mathrm{ref}}_{\mathrm{ufg},i}}, \tag{2.22}$$

where the superscript "ref" denotes quantities from the slowing-down calculation, and $q^{\mathrm{ref}}_{\mathrm{ufg},i}$ is the down-scattering source into ultrafine group ufg in region i.

The SPH iteration begins with $\mu^{(0)}_{g,i} = 1$ for all regions; for the moderator region, the factor remains fixed at unity during all iterations. At iteration l, fine-group transport in the pin is solved for the SPH-corrected system without scattering, updating the flux in region i as

$$\tilde{\phi}^{(l)}_{g,i} = \frac{\sum_j V_j \tilde{P}^{(l)}_{g,j\to i} Q^{\mathrm{ref}}_{g,j}}{V_i \mu^{(l-1)}_{g,i} \Sigma^{\mathrm{ref}}_{\mathrm{t},g,i}}, \qquad i \in \text{fuel}, \tag{2.23}$$

where $\tilde{P}^{(l)}_{g,j\to i}$ is evaluated at the corrected total cross section $\mu^{(l-1)}_{g,i}\Sigma^{\mathrm{ref}}_{\mathrm{t},g,i}$. The updated SPH factor is

$$\mu^{(l)}_{g,i} = \frac{\phi^{\mathrm{ref}}_{g,i}}{\tilde{\phi}^{(l)}_{g,i}}, \qquad i \in \text{fuel}. \tag{2.24}$$

Iterations proceed until convergence of $\mu_{g,i}$.

When applied, the SPH factors temporarily modify the transport operator: total XSs are scaled by μ before the discrete ordinates (SN) sweep, and the resulting flux solution is renormalized by the same factors immediately after the sweep. This differs from previous works [19, 20], which corrected all reaction cross sections. Those approaches treated cross sections as the quantities to be corrected, whereas the SSAPI approach instead corrects the transport operator itself—more consistent with the underlying issue, which is the misrepresentation of leakage due to missing fine-angular structure in the collision operator.

2.2 Self-Shielding Method for Non-fuel Resonances

Unlike light-water reactors, in which zirconium cladding is the primary non-fuel resonant material, advanced reactor concepts can include multiple non-fuel resonance regions depending on design choices. Neglecting these resonances can readily introduce errors of a few hundred pcm in the eigenvalue. Given this diversity and Griffin's unstructured-geometry capability, the natural initial choice was the Tone method, since it imposes no geometric restrictions, unlike classical Equivalence Theory.

The subgroup method is another geometrically flexible option, but it typically requires a heterogeneous table to generate subgroup parameters. This stems from its fixed-source formulation at each subgroup level, which is derived from the intermediate resonance (IR) model with additional simplifications that neglect resonance scattering in both the source and collision terms. As a consequence, only absorption and the λ potential XSs appear in the collision term. Physically, this causes neutrons to "see" the resonance region as less optically thick, which overestimates the escape probability; in turn, the escape XS and ultimately the absorption XS are also overestimated. This behavior has been reported in References [21, 22], and the analysis in Reference [22] identified the core issue as the omission of the resonance scattering XS in the fixed-source formulation.

Because of this built-in bias, the subgroup (or Embedded Self-Shielding Method (ESSM) [23]) approach is effectively forced to rely on an *enforced* equivalence: subgroup parameters (or an effective XS / RI table) are generated for the *target heterogeneous configuration* using the same biased fixed-source formulation, and effective XSs are later retrieved by repeating that biased calculation. Practically, this shifts a heavy burden to users, who must prepare problem-dependent heterogeneous tables. Moreover, generating those tables is nontrivial: it requires choosing representative configurations, producing reference XSs via Monte Carlo or deterministic slowing-down in heterogeneous geometry, and computing background XSs with the fixed-source formulation.

For these reasons, although a Tone implementation using heterogeneous XS tables was described in the FY21 report [3], it has not been a practical option for users due to the lack of a supported heterogeneous-table generation workflow in Griffin. Instead, in FY25 we focused on supporting the Tone method with a *homogeneous* RI table. This is feasible because the Tone method has demonstrated strong performance for fast reactor applications without pre-generated heterogeneous tables. The purpose of the Tone method in SSAPI is not for resonances of heavy isotopes in fuel regions but for those of intermediate and light mass isotopes in non-fuel regions, where the narrow resonance (NR) approximation of the Tone method works well. Critically for Griffin, this approach is intrinsically compatible with unstructured geometry and frees users from problem-specific RI table generation.

Despite these advantages, a notable drawback of the homogeneous-RI-table Tone approach is its computational cost: for each resonant isotope and resonance energy group, fixed-source solves are required (roughly twice the average number of iterations needed to converge the escape XS). To mitigate this burden, in FY25 we also pursued a substantially faster alternative with somewhat reduced geometric generality, based on an Equivalence-Theory framework using a Dancoff-category treatment and homogeneous RI tables. Not a conventional Equivalence Theory, this approach was improved by incorporating the bell-function-based Dancoff correction concept described in the previous subsection for fuel resonance treatment. This enhancement significantly improves accuracy compared to conventional Equivalence Theory while retaining its efficiency advantage.

It should be emphasized, however, that this new approach does not simply replace the Tone method. Both are retained as complementary options. The Tone method remains the most flexible and physically rigorous choice for arbitrary geometries, while the DCET, enhanced in FY25 with the bell-function-based Dancoff correction, provides a much faster alternative for problems with well-defined pin structures such as heat-pipe or moderator pins. In such cases, it achieves accuracy comparable to Tone but at a fraction of the computational cost, making it a practical substitute.

2.2.1 Advanced Homogeneous RI Table Generation

In the effort to make Tone work with the homogeneous RI table, the relationship between XSs and RIs was formulated slightly differently from the conventional practice, where resonance scattering is usually ignored. In SSAPI, resonance scattering is retained because its inclusion adds little complexity while offering the potential benefit of more accurately capturing flux depression through the denominator of the flux model. Since this formulation is not conventional, this subsection derives the relationship between effective XS and RI and the calculation method of the RI table.

SSAPI assumes the IR approximation, which employs the following spectrum model in a zero-dimensional (0D) problem:

$$\phi(E) = \frac{\phi^\infty}{E}\frac{\sum_k N^k \lambda^k(E)\sigma_\mathrm{p}^k}{\sum_k N^k\big(\sigma_\mathrm{a}^k(E) + \lambda^k(E)\sigma_\mathrm{s}^k(E)\big)}, \tag{2.25}$$

where ϕ^∞ is the asymptotic flux at much higher energy than the target resonance energy E, and $\lambda^k(E)$ is the IR parameter of isotope k. Note that λ has energy dependence here, which later introduces energy-group dependence.

Unlike conventional practice, $\sigma_\mathrm{s}^k(E)$ is not ignored. To remain consistent with the conventional form, where RI is defined as a function of background XSs, Eq. (2.25) is recast as

$$\phi(E) = \frac{\phi^\infty}{E}\frac{\sum_k N^k \lambda^k(E)\sigma_\mathrm{p}^k}{\sum_k N^k\big(\sigma_\mathrm{a}^k(E) + \lambda^k(E)\Delta\sigma_\mathrm{s}^k(E) + \lambda^k(E)\sigma_\mathrm{p}^k\big)}, \tag{2.26}$$

where $\Delta\sigma_\mathrm{s}^k(E) = \sigma_\mathrm{s}^k(E) - \sigma_\mathrm{p}^k$. Rearranging this for a target resonant isotope r yields

$$\phi^r(E) = \frac{\phi^\infty}{E}\frac{\sigma_\mathrm{b}^r(E)}{\sigma_\mathrm{a}^r(E) + \lambda^r(E)\Delta\sigma_\mathrm{s}^r(E) + \sum_{k\neq r}\big(\sigma_\mathrm{a}^k(E) + \lambda^k(E)\Delta\sigma_\mathrm{s}^k(E)\big) + \sigma_\mathrm{b}^r(E)} \tag{2.27}$$

with the background XS

$$\sigma_\mathrm{b}^r(E) = \sum_k \frac{N^k}{N^r}\lambda^k(E)\sigma_\mathrm{p}^k \tag{2.28}$$

Ignoring the energy dependence in λ and plugging this into the effective XS definition for reaction $x = \mathrm{a}, \Delta\mathrm{s}(\sigma_\mathrm{s} - \sigma_\mathrm{p}),$ and $\mathrm{nf}(\nu\sigma_\mathrm{f})$ gives

$$
\begin{aligned}
\sigma_{x,g}^{r} &= \frac{\int_{E_g}^{E_{g-1}} \sigma_x^r(E)\phi^r(E)dE}{\int_{E_g}^{E_{g-1}} \phi^r(E)dE}, \\
&= \frac{\int_{E_g}^{E_{g-1}} \frac{\phi^\infty}{E} \frac{\sigma_x^r(E)\sigma_{\mathrm{b},g}^r}{\sigma_{\mathrm{a}}^r(E)+\lambda_g^r\Delta\sigma_{\mathrm{s}}^r(E)+\sum_{k\neq r}\left(\sigma_{\mathrm{a}}^k(E)+\lambda_g^k\Delta\sigma_{\mathrm{s}}^k(E)\right)+\sigma_{\mathrm{b},g}^r} dE}{\int_{E_g}^{E_{g-1}} \frac{\phi^\infty}{E} \frac{\sigma_{\mathrm{b},g}^r}{\sigma_{\mathrm{a}}^r(E)+\lambda_g^r\Delta\sigma_{\mathrm{s}}^r(E)+\sum_{k\neq r}\left(\sigma_{\mathrm{a}}^k(E)+\lambda_g^k\Delta\sigma_{\mathrm{s}}^k(E)\right)+\sigma_{\mathrm{b},g}^r} dE}, \\
&= \frac{\int_{E_g}^{E_{g-1}} \frac{\phi^\infty}{E} \frac{\sigma_x^r(E)\sigma_{\mathrm{b},g}^r}{\sigma_{\mathrm{a}}^r(E)+\lambda_g^r\Delta\sigma_{\mathrm{s}}^r(E)+\sum_{k\neq r}\left(\sigma_{\mathrm{a}}^k(E)+\lambda_g^k\Delta\sigma_{\mathrm{s}}^k(E)\right)+\sigma_{\mathrm{b},g}^r} dE}{\int_{E_g}^{E_{g-1}} \frac{\phi^\infty}{E} \left(1-\sum_k \frac{\sigma_{\mathrm{a}}^k(E)+\lambda_g^k\Delta\sigma_{\mathrm{s}}^k(E)}{\sigma_{\mathrm{a}}^k(E)+\lambda_g^k\Delta\sigma_{\mathrm{s}}^k(E)+\sum_{k'\neq k}\left(\sigma_{\mathrm{a}}^{k'}(E)+\lambda_g^{k'}\Delta\sigma_{\mathrm{s}}^{k'}(E)\right)+\sigma_{\mathrm{b},g}^k}\right) dE},
\end{aligned}
\tag{2.29}
$$

Defining the RI as

$$
\mathrm{RI}_{x,g}^r(\sigma_{\mathrm{b},g}^r) \equiv \int_{E_g}^{E_{g-1}} \frac{\phi^\infty}{E} \frac{\sigma_x^r(E)\sigma_{\mathrm{b},g}^r}{\sigma_{\mathrm{a}}^r(E)+\lambda_g^r\Delta\sigma_{\mathrm{s}}^r(E)+\sigma_{\mathrm{b},g}^r} dE \Big/ \int_{E_g}^{E_{g-1}} \frac{\phi^\infty}{E} dE, \tag{2.30}
$$

and ignoring the energy dependence of other isotopes' XSs, Eq. (2.29) becomes

$$
\sigma_{x,g}^r = \frac{\mathrm{RI}_{x,g}^r(\sigma_{\mathrm{r,b},g}^r)\frac{\sigma_{\mathrm{b},g}^r}{\sigma_{\mathrm{r,b},g}^r}}{1-\sum_k \frac{\mathrm{RI}_{\mathrm{a},g}^k(\sigma_{\mathrm{r,b},g}^k)+\lambda_g^k\Delta\mathrm{RI}_{\mathrm{s},g}^k(\sigma_{\mathrm{r,b},g}^k)}{\sigma_{\mathrm{r,b},g}^k}}, \tag{2.31}
$$

with background XSs

$$
\sigma_{\mathrm{b},g}^r = \lambda_g^r\sigma_{\mathrm{p}}^r + \sum_{k\neq r}\frac{N^k}{N^r}\lambda_g^k\sigma_{\mathrm{p}}^k, \qquad \sigma_{\mathrm{r,b},g}^r = \lambda_g^r\sigma_{\mathrm{p}}^r + \sum_{k\neq r}\frac{N^k}{N^r}\left(\sigma_{\mathrm{a},g}^k+\lambda_g^k\sigma_{\mathrm{s},g}^k\right). \tag{2.32}
$$

The subscript r in the background XS denotes "resonance", accounting for the (removal) resonance XSs of other isotopes. Note that, in Eq. (2.31), flux depressions of other isotopes are accounted for in the IR approximation, and more importantly, resonance scattering is not ignored so that it reflects the physics more closely than the convention to ignore it.

For scattering, $\Delta\mathrm{RI}_{\mathrm{s},g}^r$ denotes the RI of the resonance scattering XS excluding the potential scattering part. It can be negative in fine groups near the resonance wing. The effective scattering XS is then given by

$$\sigma^r_{\mathrm{s},g} = \frac{\Delta \mathrm{RI}^r_{\mathrm{s},g}(\sigma^r_{\mathrm{r,b},g})}{1 - \frac{\mathrm{RI}^r_{\mathrm{a},g}(\sigma^r_{\mathrm{r,b},g}) + \lambda^r_g \Delta \mathrm{RI}^r_{\mathrm{s},g}(\sigma^r_{\mathrm{r,b},g})}{\sigma^r_{\mathrm{r,b},g}}} + \sigma^r_{\mathrm{p}}. \tag{2.33}$$

For generating an RI table, a 0D problem is solved with a single resonant isotope r and a non-resonant background isotope b, therefore $\sigma^r_{\mathrm{r,b},g} = \sigma^r_{\mathrm{b},g}$. Hydrogen is used as the background isotope since its IR parameter is unity by definition. Then, for a given background XS σ_0, $N^r = 1$, and thus $N^{\mathrm{H}} = \frac{\sigma_0}{\sigma^{\mathrm{H}}_{\mathrm{p}}}$. Solving the 0D slowing down problem for each background XS yields effective XSs $\sigma^r_{\mathrm{a},g}(\sigma_0)$, $\sigma^r_{\mathrm{s},g}(\sigma_0)$, and $\sigma^r_{\mathrm{f},g}(\sigma_0)$, which are converted into RIs as

$$\begin{aligned}
\mathrm{RI}^r_{\mathrm{a},g}(\sigma_0) &= \frac{\sigma^r_{\mathrm{a},g}(\sigma_0)}{1 + \frac{\sigma^r_{\mathrm{a},g}(\sigma_0) + \lambda^r_g(\sigma^r_{\mathrm{s},g}(\sigma_0) - \sigma^r_{\mathrm{p}})}{\lambda^r_g \sigma^r_{\mathrm{p}} + \sigma_0}}, \\
\Delta \mathrm{RI}^r_{\mathrm{s},g}(\sigma_0) &= \frac{\sigma^r_{\mathrm{s},g}(\sigma_0) - \sigma^r_{\mathrm{p}}}{1 + \frac{\sigma^r_{\mathrm{a},g}(\sigma_0) + \lambda^r_g(\sigma^r_{\mathrm{s},g}(\sigma_0) - \sigma^r_{\mathrm{p}})}{\lambda^r_g \sigma^r_{\mathrm{p}} + \sigma_0}}, \\
\mathrm{RI}^r_{\mathrm{nf},g}(\sigma_0) &= \frac{\nu \sigma^r_{\mathrm{f},g}(\sigma_0)}{1 + \frac{\sigma^r_{\mathrm{a},g}(\sigma_0) + \lambda^r_g(\sigma^r_{\mathrm{s},g}(\sigma_0) - \sigma^r_{\mathrm{p}})}{\lambda^r_g \sigma^r_{\mathrm{p}} + \sigma_0}}.
\end{aligned} \tag{2.34}$$

It should be noted that the λ potential XS of the target isotope is not included in this background XS definition and should be excluded in the usage stage as well.

Fig. 2.4 illustrates absorption and resonance scattering RI curves for large resonance of ^{89}Y at 2.6 keV. To ensure smoothness, as shown in Fig. 2.5, the SSAPI multigroup library generation code adaptively refines the background XS grid using an interval-halving algorithm from a given set of background XSs in GENDF generated through PyNJOY [24]. A default list of background XSs is provided for each isotopes in the Python script. If the relative interpolation error at the geometric mean of a segment exceeds 1%, the interval is subdivided until the tolerance is satisfied. It is seen that the interpolation error can exceed 10% if not careful about the background XS grid points.

To use this RI table, background XS of each isotope at each region for each resonance energy group is calculated by adding composition background XS and escape XS and used for interpolation from the table. For better interpolation, the cubic spline interpolation is used for the logarithmic value of background XS and linear value of RI. The escape XS calculation will be described using two different methods, Tone and Equivalence Theory, in the next subsections.

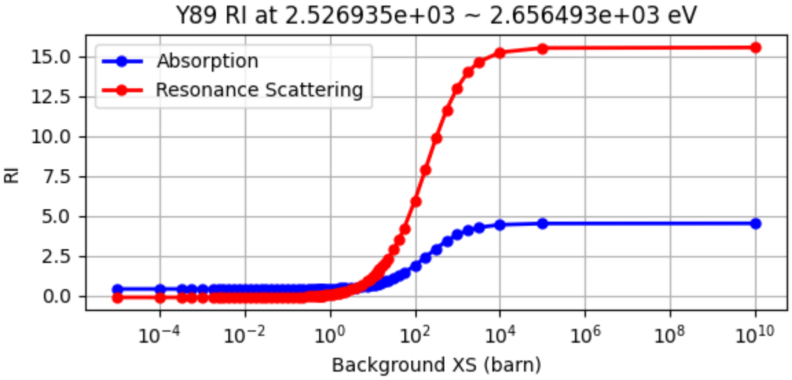

Figure 2.4. Example absorption and resonance scattering RI curves for the large resonance of ^{89}Y at 2.6 keV.

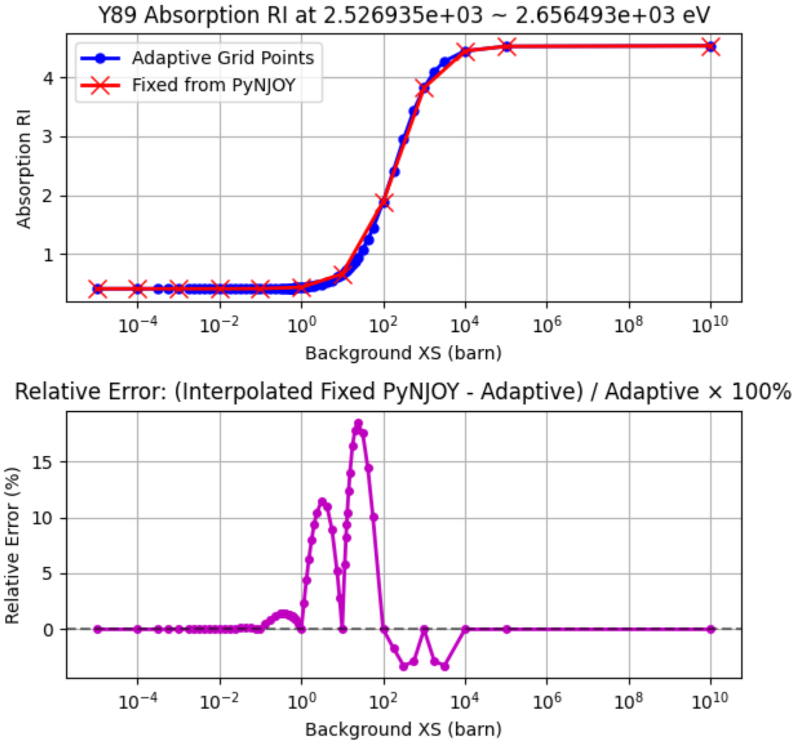

Figure 2.5. Adaptive generation of RI curves in SSAPI: (top) dilution points selected automatically, (bottom) interpolation error compared to fixed-point grids from PyNJOY.

2.2.2 Tone Method

The Tone method was originally developed for self-shielding calculation for fast reactor as the table look-up method [25]. Unlike Equivalence Theory which resorts to rational approximation of escape probability for a typical (slab, cylinder, and sphere) geometry type, interim background XS is calculated by explicitly calculating collision probabilities as

$$\sigma'^{r}_{0,g,i} = \frac{\sum_j V_j P_{g,j\to i} \sum_{k\neq r} N^k_j \sigma^k_{\mathrm{t},g,j}}{\sum_j V_j P_{g,j\to i} N^r_j}, \tag{2.35}$$

where i and j denote region, r and k denote isotope, and g is resonance energy group.

The detailed derivation of Eq. (2.35) is not given here, but there are two main approximations: the NR approximation for the scattering source and the approximation that the effect of within-group XS variation of the target isotope in regions other than the target region on the escape XS of the target region is neglected but considering only the self-shielded single value in other regions is sufficient. The former is a good approximation for high energy resonances of intermediate and light mass isotopes. The latter is not too bad approximation either since the main effect comes from the target region, and even for the secondary effect from the other region, at least averaged self-shielded value is considered (not entirely neglecting the resonance and using potential XS).

Eq. (2.35) means that the Tone method is much flexible in terms of geometry treatment as long as these collision probabilities are calculated. Modern transport codes such as Griffin do not use CPM, however. Fortunately, each of numerator and denominator can be obtained in an alternative manner using a solution of other types of transport solvers such as SN or method of characteristics (MOC) [8]. By solving the following two fixed source problems for each resonance group g,

$$\vec{\Omega}\cdot\vec{\nabla}\psi^r_g(\vec{r},\vec{\Omega}) + \Sigma_{\mathrm{t},g}(\vec{r})\psi^r_g(\vec{r},\vec{\Omega}) = \frac{1}{4\pi}S^r_g(\vec{r}), \quad \begin{cases} S^r_{g,1}(\vec{r}) = \sum_{k\neq r} N^k(\vec{r})\sigma^k_{\mathrm{t},g}(\vec{r}), & \text{for numerator,} \\ S^r_{g,2}(\vec{r}) = N^r(\vec{r}), & \text{for denominator,} \end{cases} \tag{2.36}$$

where superscript r in ψ and S indicates that these two equations are for resonant isotope r, Eq. (2.35) can be calculated by taking the ratio of two scalar flux solutions, $\phi^r_{g,1}(\vec{r})/\phi^r_{g,2}(\vec{r})$. Then, the escape XS for isotope r is obtained by

$$\sigma^r_{\mathrm{e},g,i} = \sigma'^r_{0,g,i} - \sum_{k\neq r} \frac{N^k_i \sigma^k_{\mathrm{t},g,i}}{N^r_i}, \tag{2.37}$$

and the background XSs are calculated as

$$\sigma^r_{0,g,i} = \frac{\sum_{k\neq r} N^k_i \lambda^k_g \sigma^k_{\mathrm{p}}}{N^r_i} + \sigma^r_{\mathrm{e},g,i}, \qquad \sigma^r_{\mathrm{r},0,g,i} = \frac{\sum_{k\neq r} N^k_i (\sigma^k_{\mathrm{a},g,i} + \lambda^k_g \sigma^k_{\mathrm{s},g,i})}{N^r_i} + \sigma^r_{\mathrm{e},g,i}, \tag{2.38}$$

for use in the RI table interpolation. Once RI values are interpolated, the self-shielded XSs are calculated using Eq. (2.31).

It should be noted that, since the total XSs in the collision and source terms in Eq. (2.36) and Eq. (2.37) are the self-shielded quantities evaluated at the background XS, the escape XSs are obtained through iterations between these two equations. In practice, two to three iterations are typically sufficient for convergence. An additional and important advantage is that the fixed-source formulation of Eq. (2.36) avoids the significant bias observed in the conventional subgroup method or ESSM, since it employs the macroscopic total cross section in the collision term. This ensures that the physical escape probability is evaluated accurately.

In SSAPI, Eq. (2.37) and Eq. (2.38) are implemented with a modification designed to reduce the number of fixed-source calculations. Specifically, Eq. (2.37) is approximated as

$$\frac{\sum_j V_j P_{g,j\to i} \sum_{k\neq r} N^k_j \sigma^k_{\mathrm{t},g,j}}{\sum_j V_j P_{g,j\to i} N^r_j} - \sum_{k\neq r} \frac{N^k_i \sigma^k_{\mathrm{t},g,i}}{N^r_i} \;\approx\; \frac{\sum_j V_j P_{g,j\to i} \sum_k N^k_j \sigma^k_{\mathrm{t},g,j}}{\sum_j V_j P_{g,j\to i} N^r_j} - \sum_k \frac{N^k_i \sigma^k_{\mathrm{t},g,i}}{N^r_i},$$

so that the first fixed-source problem no longer depends on isotope. Accordingly, the $S_{g,1}$ term becomes

$$\sum_k N^k(\vec{r}) \sigma^k_{\mathrm{t},g}(\vec{r}).$$

With this formulation, the number of fixed-source problems is reduced by (number of resonance isotopes$-$1) per resonance group, almost halving the original total count. Numerical tests confirmed that this approximation does not introduce any noticeable bias.

While this method offers excellent flexibility for arbitrary geometries, its main drawback is the computational cost even with this optimization. The number of fixed-source problems scales as

$$(\text{resonance groups})\times(1 + \text{resonant isotopes in the domain})\times(\text{average iterations to converge escape XSs}).$$

For a heat-pipe–cooled core problem, this amounts to roughly 25% of the total computational time, with some variation across different cases. Although this fraction is comparable to the typical share of self-shielding in lattice or direct whole-core transport calculations, the alternative method developed in FY25 achieves nearly the same accuracy at a fraction of the cost, reducing the time portion to less than 1%, though at the expense of reduced geometric flexibility. This improved method is described in the next subsection.

2.2.3 Dancoff Category-based Equivalence Theory using Bell Function

As a faster alternative, the Equivalence Theory method was implemented with improvements based on the Bell function concept described in Section 2.1.3. The main motivation is that the Tone method for non-fuel resonance treatment requires two or more orders of magnitude more computational time than the slowing-down calculations for fuel resonance treatment, making it undesirable to spend so much additional time on effects that are comparatively less important. For non-fuel pins with regular pin-type structures, such as heat pipes or metal hydride moderator pins in HPMR, the Equivalence Theory method is a natural fit because each resonant region can be treated as a single region (rather than multiple rings, e.g., in a heat pipe), and the geometry is cylindrical. Annular ring geometries, such as cladding, are also supported.

The primary advantage of the Equivalence Theory method is efficiency: only a small number of fixed-source calculations are required to evaluate Dancoff factors, since gray resonances are not numerically evaluated through fixed source calculations as in the Tone method. The trade-off, however, is the simplifying assumption that each resonant region experiences the same optical thickness for other resonant regions when calculating the escape probability of the region of interest at gray resonances. This assumption generally holds well if heat pipes are modeled as homogenized compositions and the isotope number densities in different heat pipes are uniform throughout the domain, because the composition of heat pipes is effectively constant over the core lifetime. The same reasoning applies to other non-fuel regions.

The first step is the Dancoff factor calculation using the ENCM method. Unlike in the fuel region, it is necessary to determine which regions should be treated as black. Initially, black regions are identified for each resonant isotope (i.e., the region containing the target isotope is set as black), under the assumption that resonances of different isotopes do not overlap. If different isotopes share the same black-region configuration, the fixed-source problem is identical for them, and therefore fixed-source calculations are only required for the unique black configurations. Fuel regions are always non-black unless they contain a non-negligible amount of the target non-fuel resonant isotope.

For example, in a lattice comprising a fuel rod, potassium-based homogenized heat pipe, and YH_2 moderator rod surrounded by stainless steel cladding, the number of unique black configurations (Dancoff categories) is three, as illustrated in Table 2.1. This means that only three fixed-source problems must be solved, compared to roughly 2,000 fixed-source problems for the Tone method (31 resonance groups × (1 + 26 isotopes) × ∼2 iterations).

Table 2.1. Dancoff Category Table for Total 26 Resonant Isotopes (O = Isotope Present ≡ black region, X = Not Present)

Isotopes	YH_2 Rod	YH_2 Cladding	Heat Pipe	Dancoff Category ID
^{29}Si, ^{30}Si, ^{50}Cr, ^{52}Cr, ^{53}Cr, ^{54}Cr, ^{55}Mn, ^{54}Fe, ^{56}Fe, ^{57}Fe, ^{58}Fe, ^{58}Ni, ^{60}Ni, ^{61}Ni, ^{62}Ni, ^{64}Ni, ^{92}Mo, ^{94}Mo, ^{95}Mo, ^{96}Mo, ^{97}Mo, ^{98}Mo, ^{100}Mo	X	O	O	1
^{39}K, ^{41}K	X	X	O	2
^{89}Y	O	X	X	3

It should also be noted that different isotopes in the same region can yield different Dancoff factors: for instance, potassium versus other isotopes in the heat pipe (Table 2.1). This differs from the conventional Equivalence Theory method, where the Dancoff factor is determined solely on a region-wise basis. Physically, this refinement means that potassium resonances are assumed not to overlap with those of other isotopes in the heat pipe, so that at potassium resonances neutrons see different black regions than at resonances of other isotopes.

Dancoff factor evaluation can be viewed as a type of escape probability evaluation in the black limit (though strictly speaking it is not). For grey resonances, the conventional practice is to approximate the analytic escape probabilities of the isolated region with an N-term rational form and then apply a correction to account for the shadowing effect. The one-term version is simply referred to as the Dancoff correction, while the two- or three-term versions are known as (generalized) Stamm'ler's corrections. In more advanced methods, the escape probabilities are evaluated numerically in the lattice directly at several grey resonances by performing fixed-source calculations.

SSAPI converts the analytic or numerical escape probabilities of the isolated region, which are simple CP integrations, into a one-term rational form with a bell factor that exactly preserves the analytic quantity. Because the form is one-term rational, applying the Dancoff correction is straightforward. This approach is more accurate than the N-term approximation, as it retains the analytic escape probability. Since pre-tabulated bell factors (Fig. 2.3) are available for cylinder, sphere, and slab geometries, or can be computed on the fly for annular geometries such as cladding, the method is essentially cost-free.

For an isolated lump l that belongs to a Dancoff category c (a region may belong to different lumps for different categories), the self-collision probabilities are numerically calculated at 21 hard-wired optical thickness values τ_j between 10^{-3} and $\sim 10^4$. These are obtained by back-calculating total cross sections from the given τ_j and the average chord length of the lump, and then transformed into bell factors:

$$a_{\mathrm{B}}^{c,l}(\tau_j) = \tau_j \frac{1 - P_{\mathrm{e}}^{c,l}(\tau_j)}{P_{\mathrm{e}}^{c,l}(\tau_j)}, \qquad j = 1, \ldots, 21, \quad \text{for lump } l \in \text{ Dancoff category } c. \tag{2.39}$$

If the lump is a cylinder, sphere, or slab, the pre-tabulated values (Fig. 2.3) are retrieved and the numerical CP calculation is skipped.

Next, looping through the non-fuel resonant regions, for isotope r in region i, the following escape cross section table is constructed at the 21 optical thickness points:

$$\Sigma_{\mathrm{e,table}}^{r}(\tau_j) = \frac{a_{\mathrm{B}}^{c,l}(\tau_j) D^{c,l}}{a_{\mathrm{B}}^{c,l}(\tau_j)(1 - D^{c,l}) + D^{c,l}} \Big/ \bar{l}^{c,l}, \qquad j = 1, \ldots, 21, \quad \text{for } c \ni r \text{ and } l \ni i. \tag{2.40}$$

The dependence of the average chord length on Dancoff category arises because different categories have different black lumps. This table, covering all isotopes in region i, is passed to the routine that evaluates effective XSs using the Bondarenko iteration. At each iteration, the isotope-dependent macroscopic escape cross section is computed as

$$\Sigma^r_{\mathrm{e},g,i} = \Sigma^r_{\mathrm{e,table}}\left(\Sigma_{\mathrm{t},g,i}\bar{l}^{c\ni r,l\ni i}\right), \tag{2.41}$$

where $\Sigma_{\mathrm{t},g,i}$ is the self-shielded macroscopic total cross section from the previous iteration, common to all isotopes. The isotope dependence arises through the average chord length of the lump.

From this, the background cross sections are computed for interpolation of the RI tables to obtain effective cross sections via Eq. (2.31):

$$\sigma^r_{0,g,i} = \frac{\sum_{k\neq r} N^k_i \lambda^k_g \sigma^k_{\mathrm{p}} + \Sigma^r_{\mathrm{e},g,i}}{N^r_i}, \qquad \sigma^r_{\mathrm{r},0,g,i} = \frac{\sum_{k\neq r} N^k_i \left(\sigma^k_{\mathrm{a},g,i} + \lambda^k_g \sigma^k_{\mathrm{s},g,i}\right) + \Sigma^r_{\mathrm{e},g,i}}{N^r_i}. \tag{2.42}$$

The updated self-shielded absorption and scattering cross sections are then used to recompute the macroscopic total cross section $\Sigma_{\mathrm{t},g,i}$ in Eq. (2.41), feeding the next Bondarenko iteration until convergence. Typically, 5 to 6 iterations suffice, while sometimes more than 10 iterations are required for large resonances.

3. Considerations in Pebble-bed Cross Section Generation

This section describes additional considerations in XS generation for PBRs that are useful for users to understand. Unlike prismatic-type reactors, where fuel is stationary, pebbles move and mix, and pebbles at different burnup levels coexist. Moreover, the local pebble packing fraction varies with position. Accurate self-shielding calculations and homogenized cross-section generation therefore require knowledge of the local pebble-bed configuration. The first subsection briefly explains how this information is defined and incorporated into XS generation.

Once self-shielded XSs are calculated in the detailed internal regions of pebbles and coolant using these configurations, they must be homogenized within the pebble-bed region for subsequent transport or diffusion calculations. This homogenization accounts for flux distributions across different pebble types and burnup levels, as discussed in the second subsection.

Finally, special attention is needed for streaming effects in gas-cooled PBRs. Approximately 40% of the pebble-bed region is gas, which acts essentially as a void to neutrons. In such highly voided regions, conventional homogenization models underestimate neutron diffusion and even transport because they do not capture the strong streaming effect. This underestimation reduces the predicted leakage, causing power tilts and eigenvalue errors. The third subsection presents the method developed to incorporate this streaming effect into diffusion coefficients for diffusion calculation and first order anisotropic scattering XS for transport calculation.

3.1 Defining Local Pebble-bed Configuration

For XS generation, the volume fractions of pebble ensembles of different fuel types (including dummy pebbles) and pebble burnup levels, and isotopic number densities are required. Averaging them over the entire pebble-bed region would cause large errors. Thus, the pebble-bed core is divided into several regions based on an extra element ID, “region_id,” reserved for the averaging purpose. For each of these regions, volume fractions and isotopic number densities are averaged for each pebble fuel type and burnup level and passed to SSAPI. This information is directly used in the self-shielding calculation. The volume fraction is used in the pebble macro-cell construction shown in Fig. 2.1; the composition of the outer region of a fuel zone in a pebble (`omm` in Fig. 2.1) is determined by volume homogenization of graphite layers of fuel pebbles, coolant, and any dummy pebbles. This information is also used in the TRISO-cell construction in a pebble.

It should be emphasized that this "region" concept is not the same as a spectral zone, which represents XS zones characterized by distinct spectra in the core. Instead, it is a representative region defined by pebble packing and isotopic composition. As will be explained in the next section, the spectral zone concept is not present in Griffin, as the broad-group XSs are generated for every element, and thus XSs vary continuously at element resolution. For clarity, this concept of continuously varying XSs via on-the-fly condensation has so far been demonstrated only for prismatic reactor problems, but will soon be extended to PBRs.

An additional note is needed on setting local packing fractions. The actual local packing fraction is slightly higher than the core-wide average, since pebbles cannot pack as densely near the radial boundary between the pebble-bed and reflector, and a relatively larger void exists at the top surface of the core, as shown in Fig. 3.1, where each pixel represents a chopped pineapple-shaped zone of roughly 12-cm radial and axial widths. Pebble packing is reduced by about 3–4% near the radial reflector boundary, 5–10% near the bottom reflector boundary, and 35–40% near the upper reflector boundary. These variations are inevitable because the top surface of the pebble-bed region aligns with the maximum surface of the pebbles for this model. Due to less packing near radial and axial boundaries, the pebble packing fraction in the core center is 1–4% higher than the core average. Neglecting this region dependence may lead to non-negligible effects: reduced packing in the majority of the core center decreases shadowing and increases resonance absorption, while increased fuel proximity near control rods at the top provides more source neutrons to the absorber, leading to more absorption and a lower eigenvalue.

This region-dependent pebble packing fraction can be set manually in the input file by calculating them externally, or internally by using `PorosityFromLocationFileIC`, which calculates "region_id"-averaged porosities and assigns them to a variable. However, since the latter performs high-order three-dimensional (3D) numerical integration (default = 43) in each element, it is slow and should be run only once before the actual calculation. To support faster workflows, a simple MATLAB function was written that performs only axial integration of the analytic disk area (sphere–cylinder intersection). This script executes in seconds with neglgible error and can therefore be used on-the-fly once merged into the Griffin code. Fig. 3.1 was generated using this

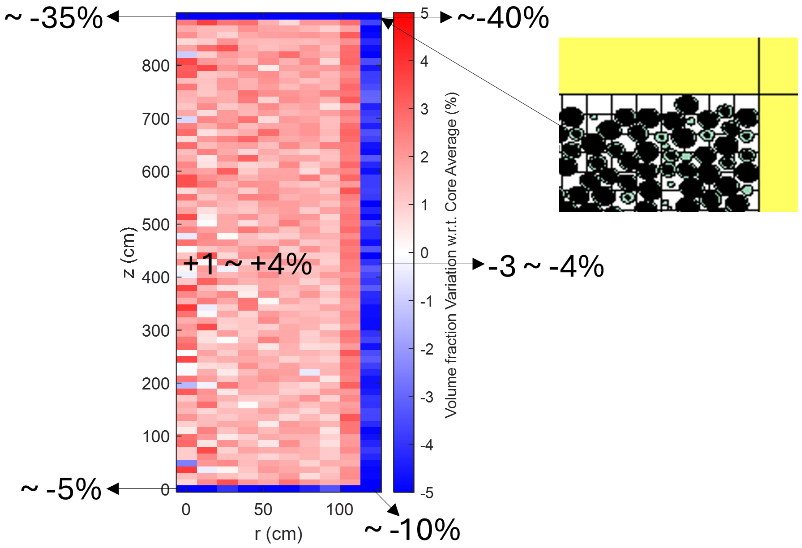

Figure 3.1. Variations of local pebble volume fractions relative to the core average.

MATLAB script.

For a fresh core where isotopic number densities of pebbles are uniform throughout the pebble bed, it is sufficient to consider only the pebble volume fractions. In such cases, two to three radial and axial regions of about twice the pebble size near the periphery, plus one interior region, are typically sufficient. How to define the regions in the top portion of the core, where a large void exists above the pebble bed, remains an open question for future work.

For depletion calculations, the local burnup distribution is calculated by the pebble depletion module [26]. The volume fraction distribution of pebble ensembles at different burnup levels must be properly resolved, which requires finer region definitions inside the core. That said, the inner regions need not be finer than the radial width of streamlines, but the optimal coarseness remains a research topic. Currently, the determination of region boundaries relies on engineering judgment based on streamline configuration.

3.2 Homogenization Method

After the self-shielding calculation is performed for each "region" explained in the previous subsection, homogenization is carried out within the same region. (Condensation is done element-wise, as explained in the next section.) For homogenization, flux-weighting factors across detailed regions within pebbles and coolant are required. Griffin employs the so-called multi-pebble model to calculate these weighting factors, instead of the effective pebble model used in legacy tools such as VSOP [27]. The multi-pebble model is particularly important when high-burnup pebbles are mixed with fresh pebbles. Simple volume-averaging of fresh and highly burned fuel compositions is not appropriate: for example, the self-shielding effect for the 1 eV resonance in ^{240}Pu is severely mistreated, leading to more than a +10% absorption rate error and a lower eigenvalue [10].

A CPM-based formulation that accounts for pebble-to-pebble interactions was developed in FY23 [10]. The following coupled balance equations for coolant and pebbles—linked through surface particle currents—are solved for each fine group:

$$\begin{aligned} J_x^- &= E_{\mathrm{c}\to x} V_\mathrm{c} F_\mathrm{c} + \sum_y T_{y\to x} J_y^+ , \\ J_x^+ &= \sum_i E_{x,i} V_{x,i} F_{x,i} + T_x J_x^- , \\ V_\mathrm{c} \Sigma_\mathrm{c} \phi_\mathrm{c} &= P_{\mathrm{c}\to\mathrm{c}} V_\mathrm{c} F_\mathrm{c} + \sum_x \gamma_{x\to\mathrm{c}} J_x^+ , \\ V_{x,i} \Sigma_{x,i} \phi_{x,i} &= \sum_j P_{x,j\to i} V_{x,j} F_{x,j} + \gamma_{x,i} J_x^- , \end{aligned} \tag{3.1}$$

where i and j denote internal pebble regions, c indicates coolant, and x and y refer to pebble types. Here, f_x is the fraction of the total surface area of pebble type x relative to all pebble types, F is the volumetric source (including self-scattering), $P_{x,i\to j}$ is the collision probability from region i to j within pebble type x, $\gamma_{x\to\mathrm{c}}$ is the probability that neutrons leaving pebble type x first collide in the coolant, $\gamma_{x,i}$ is the first-flight blackness in internal region i of pebble type x, E is the escape probability (reciprocal to γ), and $T_{x\to y}$ is the transmission probability between pebble types x and y.

The most important point is that the XSs on the left-hand side of the third and fourth equations are *transport* XSs, not total XSs. This distinction is crucial for correctly capturing the streaming effect through the P. Benoist method, which will be described in the next subsection. Accordingly, the associated CP coefficients must also be evaluated using transport XSs.

The first two equations describe the balance of incoming and outgoing partial currents at pebble surfaces, while the third and fourth describe volumetric collision rates in the coolant and internal pebble regions. These equations are coupled via partial currents and fluxes. CP coefficients in the second and fourth equations are straightforward to compute using 1D numerical integration for pebble geometry, whereas those in the first and third equations involve the stochastic coolant geometry and are not directly known. To address this, a stochastic assumption is introduced: neutrons originating from pebbles or coolant are treated identically, as isotropic and uniform sources in the coolant. Under this assumption, $\gamma_{x\to c}$ and $T_{y\to x}$ lose their source dependence and reduce to $P_{\mathrm{c}\to\mathrm{c}}$ and $E_{\mathrm{c}\to x}$, respectively. Further, assuming that the fraction of neutrons reaching the surface of each pebble type from coolant escape is proportional to f_x, the first and third equations in Eq. (3.1) reduce to:

$$\begin{aligned} J_x^- &= f_x(1 - P_{\mathrm{c}\to\mathrm{c}})(V_\mathrm{c}F_\mathrm{c} + \sum_y J_y^+), \\ V_\mathrm{c}\Sigma_\mathrm{c}\phi_\mathrm{c} &= P_{\mathrm{c}\to\mathrm{c}}(V_\mathrm{c}F_\mathrm{c} + \sum_x J_x^+). \end{aligned} \tag{3.2}$$

At this stage, the key remaining task is to evaluate the coolant self-collision probability, $P_{\mathrm{c}\to\mathrm{c}}$, in order to complete all CP coefficients involving the coolant. Using the exponential chord-length distribution for the coolant region and Cauchy's formula for the mean chord length, $\bar{l}_\mathrm{c} = \frac{4V_\mathrm{c}}{\sum_y S_y}$, $P_{\mathrm{c}\to\mathrm{c}}$ is derived as:

$$P_{\mathrm{c}\to\mathrm{c}} = \frac{\bar{l}_\mathrm{c}\Sigma_\mathrm{c}}{\bar{l}_\mathrm{c}\Sigma_\mathrm{c} + 1}. \tag{3.3}$$

This coupled system is solved independently for each fine group. Since the overall system forms an eigenvalue problem, it is solved by power iteration with a group sweep. For each group with a given volumetric source, the flux solution is obtained using LU factorization, as the combined system matrix is dense. Finally, note that a specular boundary condition is assumed, corresponding to an infinite pebble bed. This assumption is reasonable for fine energy groups, within which spectral transition effects from reflectors can be neglected.

Once the flux distribution within each "region" is obtained, flux-volume homogenization is performed to generate region-averaged fine-group XSs. This procedure follows the conventional approach, except for the diffusion coefficient used in diffusion calculations and the first-order anisotropic scattering XS used in transport calculations, which are modified to account for the streaming effect as explained in the next subsection.

3.3 Streaming Correction Method

The conventional approach for calculating diffusion coefficients is to homogenize the transport cross sections and take their inverse divided by three, i.e.,

$$\overline{D}^{\text{Conv.}} = \frac{\sum_i \phi_i V_i}{3\sum_i \Sigma_{\text{tr},i}\phi_i V_i}, \tag{3.4}$$

where the transport cross section can be obtained using any transport-correction scheme such as the outflow or inflow approximation. However, this approach has long been recognized as inadequate for lattices exhibiting strong streaming effects [11, 28]. P. Benoist proposed the following alternative formulation [11]:

$$\overline{D}^{\text{Benoist}} = \frac{1}{3}\frac{\sum_i \phi_i V_i \sum_j P_{i\to j}\frac{1}{\Sigma_{\text{tr},j}}}{\sum_i \phi_i V_i}, \tag{3.5}$$

which requires collision probabilities from region i to region j. Later, J. Lieberoth and A. Stojadinovic proposed a simplified formula tailored to pebble-bed reactors [28], but their approach relies on an effective-pebble model. By contrast, the P. Benoist method is particularly well suited here because the required collision probabilities are already available from the multi-pebble CPM model described in the previous subsection. It should be noted that $P_{i\to j}$ must be evaluated using transport cross sections, for which the outflow-based transport correction is sufficient.

For transport calculations, the streaming effect is represented through enhanced anisotropic scattering. Specifically, the first-order self-scattering cross section is increased by the difference between the conventional and Benoist-based transport cross sections:

$$\overline{\Sigma}^{1,\text{Benoist}}_{\text{s},g\to g} = \overline{\Sigma}^{1}_{\text{s},g\to g} + \overline{\Sigma}^{\text{Conv.}}_{\text{tr},g} - \frac{1}{3\overline{D}^{\text{Benoist}}_{g}}. \tag{3.6}$$

Fig. 3.2 compares conventional and Benoist diffusion coefficients for a 60% pebble volume fraction. As expected, the Benoist coefficients are larger, reflecting the stronger diffusion effect associated with neutron streaming. This streaming-correction scheme was tested in a 1D cylindrical-Z problem of radius 1.2 m. Griffin power distributions obtained using SSAPI-generated cross sections, with and without streaming correction, were compared against reference Serpent2 results. As an additional check, Griffin results using Serpent-generated cross sections with and without the

Cumulative migration method (CMM) option were also compared.

The agreement was excellent: diffusion results using SSAPI matched those obtained with Serpent-generated cross sections for both corrected and uncorrected cases, confirming that the streaming-correction method described here is accurate. For transport calculations, the shift in power distribution due to streaming correction followed the same trend as in diffusion, and the corrected transport solutions matched closely with continuous-energy Serpent2 results. Finally, the comparison between diffusion and transport confirms once again that diffusion theory tends to overestimate leakage, although the magnitude of the error was small in this test problem.

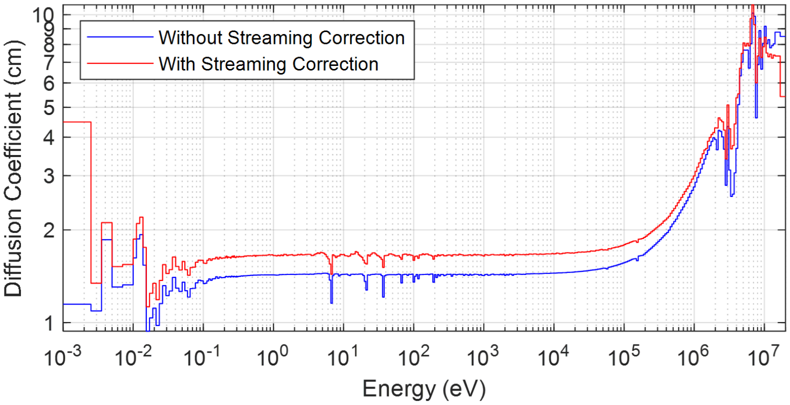

Figure 3.2. Diffusion coefficients comparison between conventional and Benoist schemes.

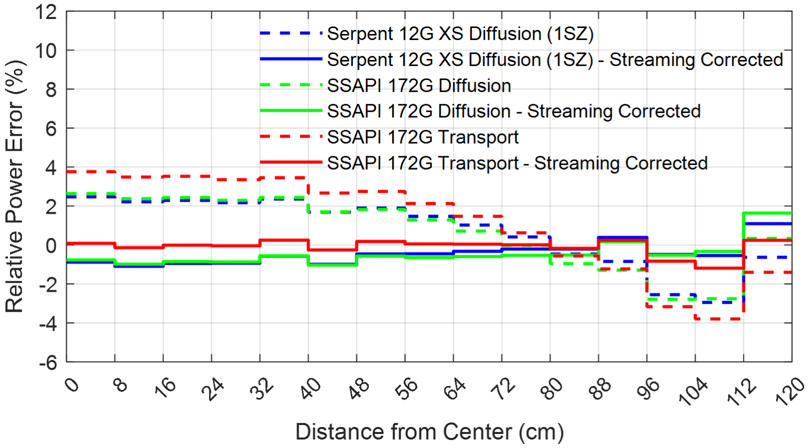

Figure 3.3. Power distribution comparison between Serpent2 and Griffin with and without streaming correction for a 1D core problem (with region-wise pebble packing fraction in SSAPI).

4. On-the-fly Condensation with Consistent P_0 Transport Correction

The procedure so far has been about to generate XSs in a fine-group structure (SSAPI multigroup library structure). Most of the lattice physics or direct whole-core transport codes use this fine-group structure to perform a heterogeneous fine-mesh transport calculation. However, it takes a significant amount of time to directly solve the whole-core problem with a fine-group fine-mesh transport calculation. Thus, an effort to save computational time was put in FY25 to devise a way to condense fine-group XS into a broad-group structure with fewer than 10 groups, without losing fine-mesh fidelity. This approach benefits applications such as micro-reactors or pebble-bed reactors, which exhibit relatively tighter core-wide spectral transition effects, making the conventional two-step procedure less straightforward and motivating direct whole-core calculation. The work was mainly inspired by the subgroup decomposition method [29], but was implemented differently, with observations that differ from those in Reference [29]. Preliminary results are very promising, provided that the performance of the fixed-source discontinuous finite element method (DFEM)-SN solver is improved. The following subsection explains the theory and implementation, followed by verification results.

4.1 Theory and Implementation

The main idea is to iteratively solve a broad-group eigenvalue problem with fine-group fixed-source problems which provides the condensation spectrum to update broad-group XS. The energy–angle correlation in the condensation is accounted for via the consistent P_0 transport correction. Although exact reaction-rate preservation is not achieved unless the correction order approaches infinity (unlike in acceleration schemes such as coarse-mesh finite difference (CMFD)), the results should be close enough in the first few correction orders.

The following procedure is applied during the flux calculation after the self-shielding calculation. At the n'th outer iteration (Richardson or non-linear Newton iteration) of a broad-group eigenvalue solve, the sequence is as follows:

1. **Prolongation of element-wise flux moments**

   The first step is the prolongation of broad-group flux moments into fine-group flux moments for each element. Broad-group spherical harmonics moments of the previous outer iteration are averaged on each element and converted into Legendre moments as

$$\phi_{e,G,l}^{(n-1)} = \sqrt{\sum_{m=-l}^{l} \left(\phi_{e,G,l,m}^{(n-1)}\right)^2}, \qquad \phi_{e,G,l,m}^{(n-1)} = \frac{\sum_{q\in e} w_q \phi_{q,G,l,m}^{(n-1)}}{\sum_{q\in e} w_q}.$$

Here G is a broad-group index, l and m denote spherical harmonics order, q and e are a quadrature point and element, respectively, and w_q is a quadrature weight.

Next, fine-group spherical harmonics moments from the previous fixed-source solution are modulated based on their Legendre moments and the broad-group flux-moment solution of the eigenvalue problem:

$$\phi_{e,g,l,m}^{\mathrm{FSP}(n-\frac{1}{2})} = \frac{\phi_{e,g,l,m}^{\mathrm{FSP}(n-1)}}{\sum_{g'\in G} \sqrt{\sum_{m=-l}^{l} \left(\phi_{e,g',l,m}^{\mathrm{FSP}(n-1)}\right)^2}} \, \phi_{e,G\ni g,l}^{(n-1)}.$$

Superscript FSP stands for fixed-source problem, and g is a fine-group index. The initial value $\phi_{e,g,l,m}^{\mathrm{FSP}(0)}$ is taken from the infinite-medium k_∞ spectrum of the element's composition.

2. **Gauss–Seidel fine-group sweep using fixed-source DFEM-SN solver**

   Using these fine-group flux moments, the fine-group fission source is first evaluated:

$$Q_{\mathrm{f},e,g}^{\mathrm{FSP}(n)} = \frac{1}{k_{\mathrm{eff}}^{(n-1)}} \chi_{e,g} \sum_{g'} \nu\Sigma_{\mathrm{f},e,g'} \phi_{e,g',0,0}^{\mathrm{FSP}(n-\frac{1}{2})}.$$

   With this fission source fixed, a fine-group sweep is performed once from the lowest to highest groups in Gauss–Seidel fashion for the scattering source. Spherical harmonics moments of the fixed source are

$$Q_{e,g,l,m}^{\mathrm{FSP}(n)} = \delta_{l0}\delta_{m0} Q_{\mathrm{f},e,g}^{\mathrm{FSP}(n)} + \sum_{g'\neq g} \Sigma_{\mathrm{s},e,g'\to g,l} \phi_{e,g',l,m}^{\mathrm{FSP}(n-\frac{1}{2})}.$$

   Using this, $\phi_{e,g,l,m}^{\mathrm{FSP}(n)}$ is obtained by solving the fixed-source problem with scattering via the fixed-source DFEM-SN sweeper. Note that the thermal up-scattering iteration is not included here, but only considered through the outer iteration in the broad-group sense. The effect of adding the thermal up-scattering iteration loop will be examined in the future.

For fuel regions in resonance groups, as explained in Section 2.1.4, the SPH factors are applied: they multiply the macroscopic total XS before the sweep and are again applied to the flux solution immediately afterward to account for the angular dependence of the fine-group total XS.

3. **Update element-wise broad-group macroscopic XS with consistent P_0 transport correction**

   After the fine-group sweep, element-wise broad-group XSs are updated using the fine-group flux solution. Higher-order scattering XSs are condensed explicitly with higher-order Legendre moments, while elements with zero moments use scalar-flux weighting instead.

   The total XS in the collision term must be condensed using the angular flux spectrum, making it angle-dependent. Since the transport solver cannot handle angle-dependent total XS, the following manipulation is used:

$$\begin{aligned}\Sigma_{\mathrm{t},e,G}(\vec{\Omega})\psi_{e,G}(\vec{\Omega}) &= \sum_{g\in G}\Sigma_{\mathrm{t},e,g}\psi_{e,g}(\vec{\Omega})\\ &= \sum_{l,m}\frac{2l+1}{4\pi}\sum_{g\in G}\Sigma_{\mathrm{t},e,g}\psi_{e,g,l,m}Y_{l,m}(\vec{\Omega})\\ &\simeq \sum_{l,m}\frac{2l+1}{4\pi}\Sigma_{\mathrm{t},e,G,l}\psi_{e,G,l,m}Y_{l,m}(\vec{\Omega})\\ &= \Sigma_{\mathrm{t},e,G}\psi_{e,G}(\vec{\Omega}) + \sum_{l,m}\frac{2l+1}{4\pi}\left(\Sigma_{\mathrm{t},e,G,l}-\Sigma_{\mathrm{t},e,G}\right)\psi_{e,G,l,m}Y_{l,m}(\vec{\Omega}),\end{aligned}$$

   where the second term is shifted to the right-hand side, yielding a corrected higher-order self-scattering term:

$$\Sigma^{\mathrm{Corr.}}_{\mathrm{s},e,g\to g,l>0} = \Sigma_{\mathrm{s},e,g\to g,l>0} - \left(\Sigma_{\mathrm{t},e,G,l}-\Sigma_{\mathrm{t},e,G}\right).$$

   This is the consistent P_0 transport correction discussed in Reference [30], truncated at the maximum anisotropic scattering order of the system.

4. **Convergence check of region-wise broad-group macroscopic XS**

   Convergence of condensed broad-group XSs is checked region-wise (not element-wise). They are generated using region-averaged flux moments as condensation weights:

$$\phi_{x,g,l}^{\mathrm{FSP}(n)} = \frac{\sum_{e\in x} V_e \sqrt{\sum_{m=-l}^{l} \left(\phi_{e,g,l,m}^{\mathrm{FSP}(n)}\right)^2}}{\sum_{e\in x} V_e},$$

where x denotes a XS-region index. These moments are not used in transport calculations, but only for convergence checking. Numerical tests confirmed that scattering XSs govern the slowest convergence, and a 1% tolerance on the zeroth-moment component suffices.

This procedure is executed only until region-wise broad-group XSs converge, not until full angular flux convergence. Thus, computational time is reduced by shortening each Richardson or Newton iteration in the broad-group structure once broad-group XSs converge, assuming one-step fine-group solves take comparable time. Currently, however, the fine-group fixed-source solver differs from that in the transport solver for the eigenvalue system: it uses unaccelerated source iteration. As a result, each outer iteration takes longer than an iteration of the fine-group eigenvalue system, defeating the purpose of the approach. Performance will therefore be improved by implementing a Generalized Minimal Residual method (GMRES) solve preconditioned by diffusion synthetic acceleration (DSA), which is expected to significantly reduce cost. Verification results are presented in the next subsection.

There are two (and potentially three) differences between this scheme and the original [29]. First, the fine-group fixed-source problems here accounts for self-scattering, while the transport solve in the original is performed without self-scattering—reducing cost per iteration but increasing the number of outer iterations. Second, in the original, fixed-source problems for different fine groups are independent (Jacobi-like), with no inter-group feedback per iteration. Third, although not clearly addressed in Reference [29], broad-group XS-region definitions are element-based in this work, ensuring high fidelity.

4.2 Verification

This method was first verified using a simple pseudo-1D problem, shown in Fig. 4.1. The blue and beige circles represent a fuel rod and a helium-filled hole, respectively, and the small red dot denotes a B_4C absorber. The background medium is graphite. The left, top, and bottom boundaries are reflective, and the right boundary is a vacuum boundary condition.

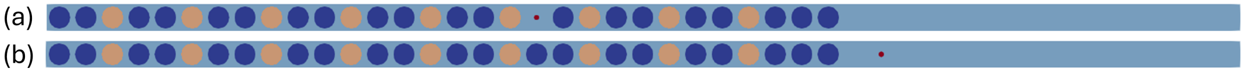

Figure 4.1. Pseudo-1D small core configuration for demonstration of the on-the-fly condensation scheme

Using the 70-group structure (WIMS 69-group [31] plus a 20 MeV upper energy boundary) as the fine group, we tested broad-group structures with 2 groups (cutoff at 0.625 eV), 4 groups (cutoffs at 0.625 eV, 148.7 eV, 821 keV), and 8 groups (cutoffs at 0.1 eV, 0.3 eV, 0.625 eV, 4 eV, 148.7 eV, 9.118 keV, 821 keV). For each broad-group structure, transport-correction orders from 0 to 3 were evaluated. All calculations enforced a 1% tolerance on P0 (0th Legendre) broad-group XSs.

Table 4.1 and Table 4.2 present the eigenvalue results for problems (a) and (b), respectively. The G2/TcP0 case—two groups without transport correction—substantially overestimates the eigenvalue: +520 pcm for problem (a) and +1305 pcm for problem (b). This bias stems from underestimated leakage, as indicated in Fig. 4.2, where power is higher at the center and lower at the periphery. The transport correction increases the modeled leakage. Most of the error is removed by the first-order correction, whereas second- and higher-order corrections tend to reintroduce some error for the 2-group case. The correction is not fully effective with only two groups, but errors decrease clearly as the broad-group structure is refined. The residual error drops to below 10 pcm in the 8-group (G8) case. As shown in Fig. 4.3, flux errors are nearly eliminated for G8 with TcP1. Across all broad-group structures, reflector-region fluxes are underestimated without transport correction, with larger underestimation for coarser group structures. Based on these results, an 8-group calculation with first-order transport correction appears sufficient for the cases studied.

To build additional confidence in more realistic applications, a HPMR 2D core problem in control-drum-out and control-drum-in configurations was tested. Detailed verification against continuous-energy Monte Carlo for this problem is presented in the next section, which also provides the problem specification. Table 4.3 and Table 4.4 present the results. The trends mirror

Table 4.1. Eigenvalue Error (pcm) of Different Broad-group Structures with Different Transport Correction Orders for Pseudo-1D Core Problem (a) (Ref. = 70G Calculation (0.82806))

Transport Correction Order	G2		G4		G8	
	k_{eff}	Δk_{eff} (pcm)	k_{eff}	Δk_{eff} (pcm)	k_{eff}	Δk_{eff} (pcm)
TcP0	0.83327	521	0.82866	60	0.82889	83
TcP1	0.82764	-42	0.82850	45	0.82820	14
TcP2	0.82634	-172	0.82799	-7	0.82803	-3
TcP3	0.82678	-128	0.82804	-1	0.82805	-1

Table 4.2. Eigenvalue Error (pcm) of Different Broad-group Structures with Different Transport Correction Orders for Pseudo-1D Core Problem (b) (Ref. = 70G Calculation (1.14035))

Transport Correction Order	G2		G4		G8	
	k_{eff}	Δk_{eff} (pcm)	k_{eff}	Δk_{eff} (pcm)	k_{eff}	Δk_{eff} (pcm)
TcP0	1.15340	1305	1.14237	202	1.14223	188
TcP1	1.13973	-62	1.14012	-22	1.14031	-3
TcP2	1.13941	-94	1.14002	-33	1.14030	-5
TcP3	1.13956	-78	1.14003	-32	1.14030	-5

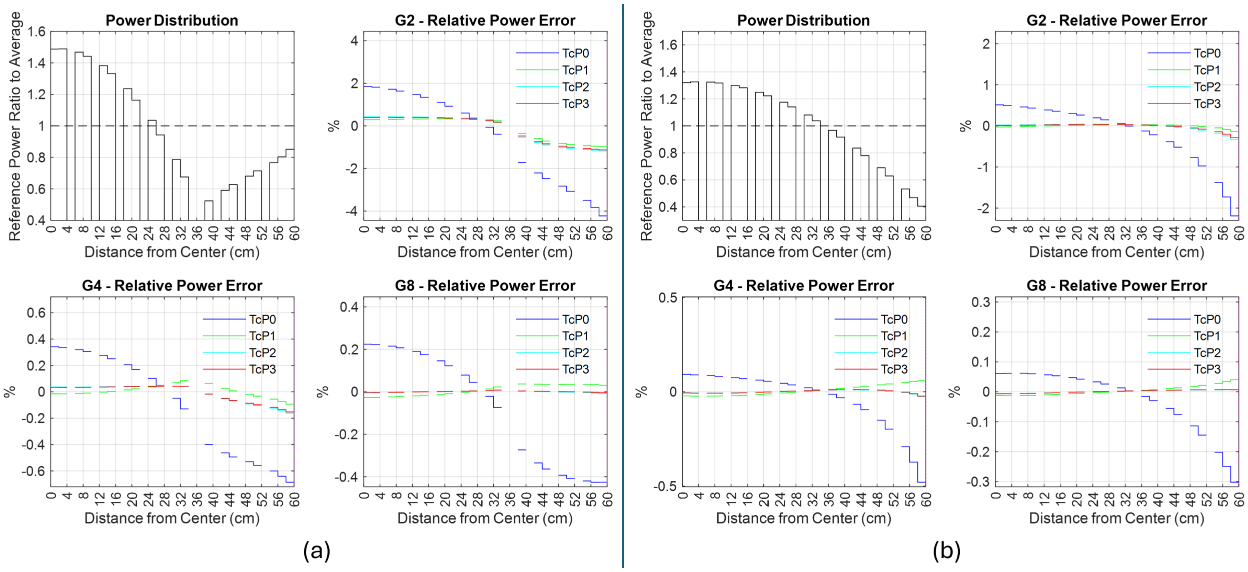

Figure 4.2. Power distribution and relative errors of the on-the-fly condensation scheme with respect to fine-group calculation

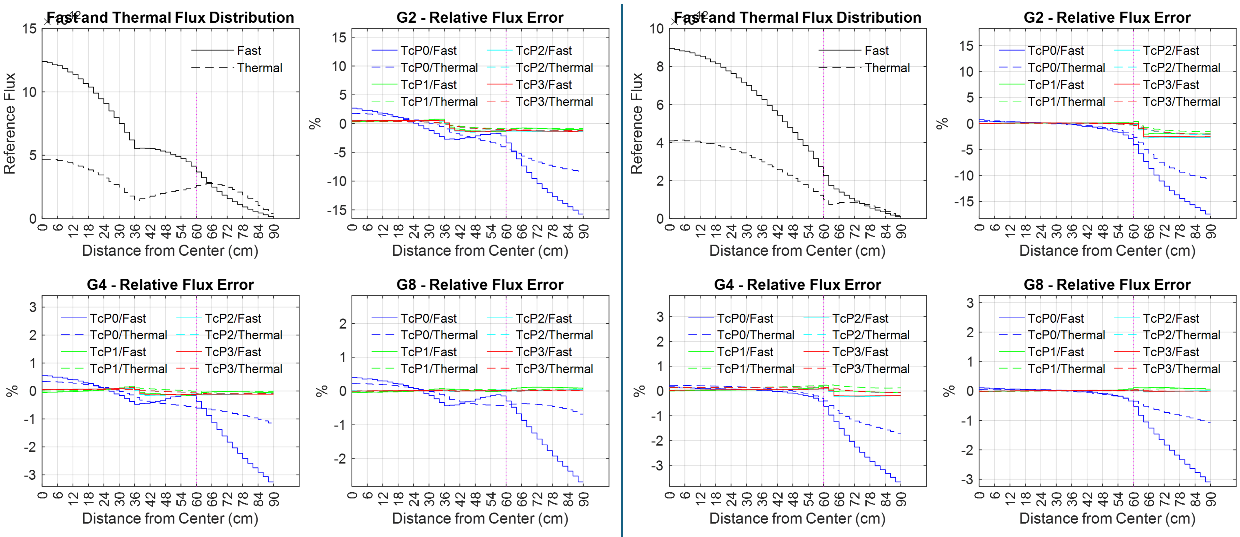

(a) (b)

Figure 4.3. Flux distribution and relative errors of the on-the-fly condensation scheme with respect to fine-group calculation

those observed in the pseudo-1D core problem: the 2-group calculation is insufficient even with higher-order transport corrections, whereas the 8-group calculation with first-order transport correction achieves good accuracy. Power-distribution errors shown in Fig. 4.4 and Fig. 4.5 support this conclusion. For both configurations, finer group structures improve the power distribution, and first-order correction performs better than no correction. This trend is more pronounced for the control-drum-in configuration; even there, the 8-group calculation with first-order transport correction provides sufficiently good accuracy.

Table 4.3. Eigenvalue Error (pcm) of Different Broad-group Structures with Different Transport Correction Orders for Control **Drum Out** Configuration of HPMR (Ref. = 70G Calculation (1.10011))

Transport Correction Order	G2		G4		G8	
	k_{eff}	Δk_{eff} (pcm)	k_{eff}	Δk_{eff} (pcm)	k_{eff}	Δk_{eff} (pcm)
TcP0	1.11441	1430	1.10436	425	1.10238	226
TcP1	1.09927	-84	1.10049	38	1.10005	-6
TcP2	1.09947	-64	1.10062	51	1.10010	-1
TcP3	1.09942	-69	1.10057	45	1.10008	-3

Table 4.4. Eigenvalue Error (pcm) of Different Broad-group Structures with Different Transport Correction Orders for Control **Drum In** Configuration of HPMR (Ref. = 70G Calculation (0.99696))

Transport Correction Order	G2		G4		G8	
	k_{eff}	Δk_{eff} (pcm)	k_{eff}	Δk_{eff} (pcm)	k_{eff}	Δk_{eff} (pcm)
TcP0	1.01032	1336	0.99969	273	0.99903	207
TcP1	0.99619	-77	0.99691	-5	0.99697	1
TcP2	0.99575	-121	0.99680	-16	0.99699	3
TcP3	0.99567	-129	0.99676	-20	0.99697	1

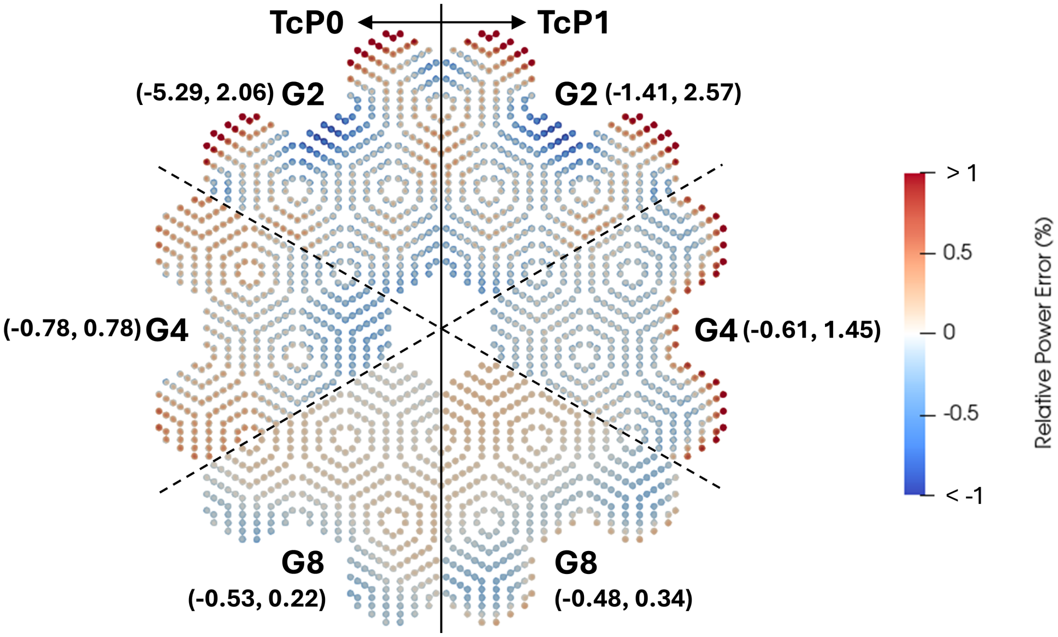

Figure 4.4. Relative error (%) of power distribution of on-the-fly condensation obtained using different broad-group structures with 0th and 1st transport correction orders for the control **drum out** configuration of HPMR.

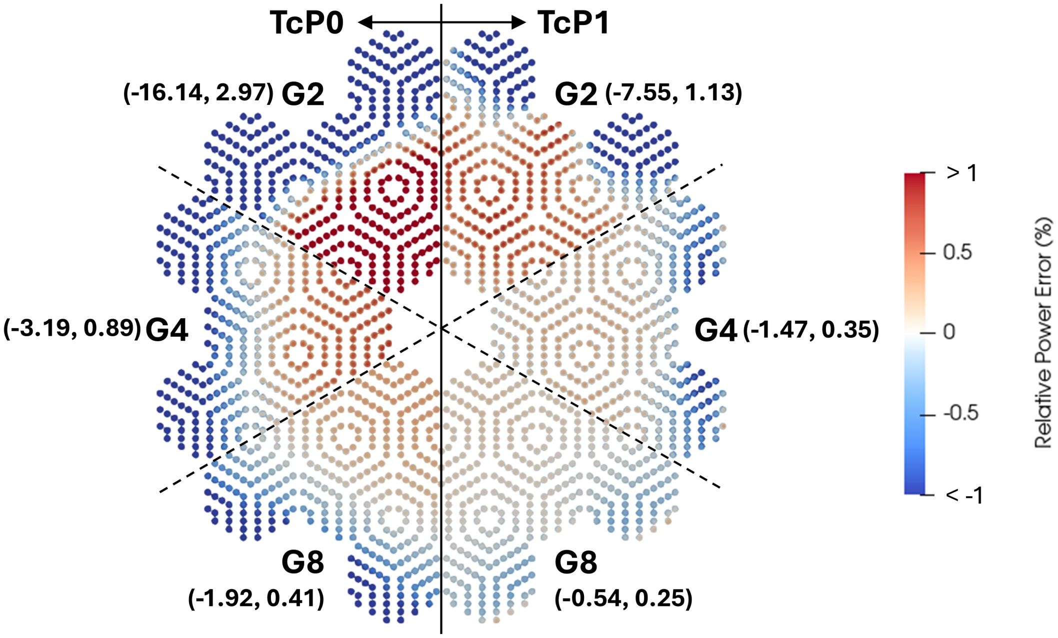

Figure 4.5. Relative error (%) of power distribution of on-the-fly condensation obtained using different broad-group structures with 0th and 1st transport correction orders for the control **drum in** configuration of HPMR.

The convergence history and computational time are summarized in Fig. 4.6. The upper panels show the residual-reduction ratio over Richardson iterations for the fine-group eigenvalue solve and for the broad-group solve with on-the-fly (OTF) condensation; the left and right columns correspond to the control-drum-out and control-drum-in configurations, respectively. In the upper figures, dashed curves with markers report the residual relative to its initial value (left y-axis), while solid curves report the eigenvalue (right y-axis). Bold markers denote iterations in which a fine-group transport sweep is performed. For example, the red X markers for "G8–OTF" appear only through the fifth Richardson iteration, indicating that the broad-group XSs converge within five iterations; from the sixth iteration onward, only the 8-group CMFD eigenvalue solve is performed.

The residual-reduction behavior in the two-group and four-group cases degrades relative to the fine-group baseline, whereas the eight-group case closely tracks the fine-group convergence. This degradation arises from slow convergence of the broad-group XSs; refining the thermal energy range (i.e., using more thermal groups) mitigates this issue substantially. This suggests that adding a thermal iteration loop within the fine-group source-update loop may be beneficial; its impact will be investigated in future work.

For the eight-group case, a speedup was anticipated because only five fine-group transport sweeps are required, versus 8–9 sweeps in the fine-group eigenvalue solve. However, as shown in the lower panels, each fine-group transport sweep per outer iteration in the fixed-source mode is roughly twice as expensive as a sweep within the fine-group eigenvalue solve. Consequently, the overall runtime is larger, despite the much faster broad-group eigenvalue solves once the broad-group XSs have converged. This outcome is attributable to the current fine-group fixed-source solver in Griffin, which uses unaccelerated source iteration. A high-priority improvement is therefore to implement a GMRES solver preconditioned with DSA. If the fixed-source performance approaches that of the fine-group CMFD system, the total computational time should decrease by roughly a factor of two (somewhat less in practice due to other cost components).

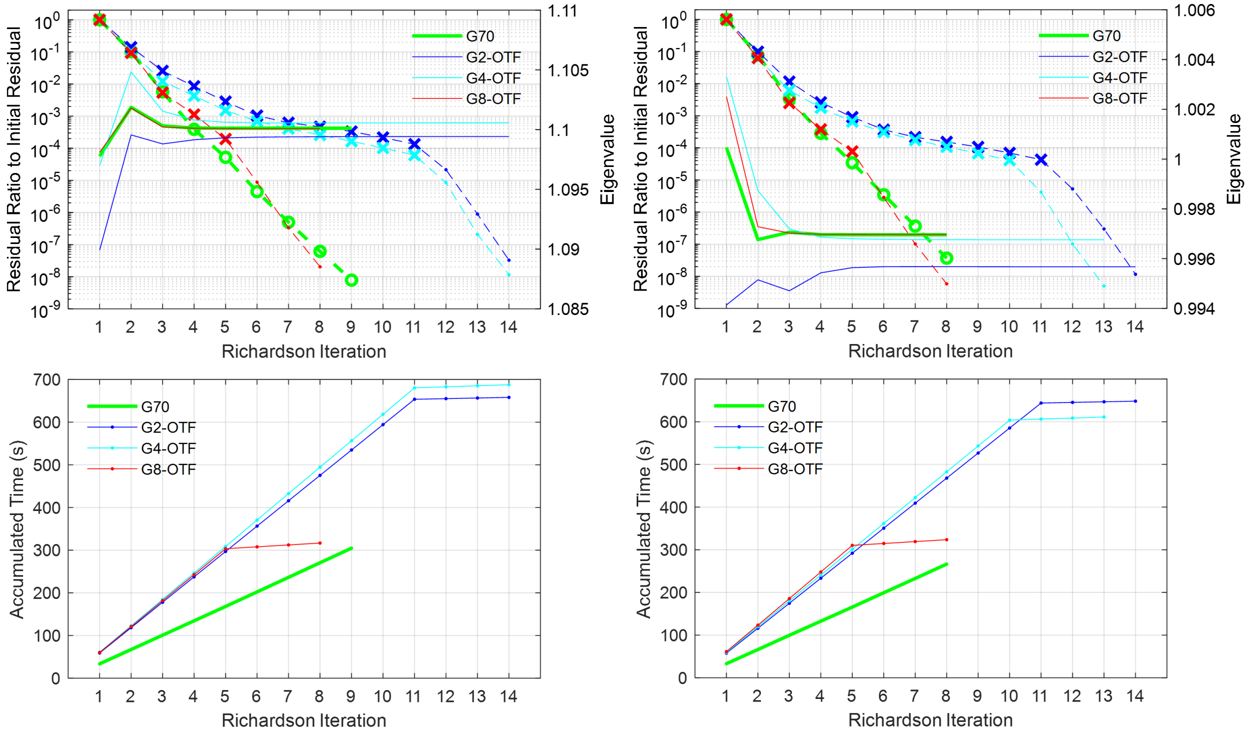

(a) CD Out

(b) CD In

Figure 4.6. Convergence history and computational time comparison between direct fine-group calculation and on-the-fly condensation for control drum out and in configurations of HPMR.

5. Verification Tests Using Core Benchmark Problems

To assess the methodologies discussed in Chapter 2 and Chapter 3, this section presents results for a set of 2D core problems: the GCMR [32] and HPMR [33] for prismatic-type reactors, and the gPBR [34] and gFHR [35] for pebble-bed reactors. For the PBR cases, the cores were simplified to 2D RZ-geometry. All of these problems are based on TRISO-bearing advanced reactor designs that are of primary interest today. The comparisons focus on eigenvalue accuracy, power distribution, and control drum or rod worths, with a brief remark on computational performance also provided.

Reference solutions were generated using the continuous-energy Monte Carlo code Serpent2 [36]. All problems were modeled under isothermal conditions at 900 K, and the ENDF/B-VII.1 library was used for both codes. Griffin calculations employed 70-group multigroup libraries generated with NJOY [37], where the group structure matches the WIMS 69-group scheme with an additional boundary at 20 MeV. DFEM-SN with CMFD acceleration was used with the 1st order anisotropic order for all problems.

5.1 GCMR Benchmark

For a gas-cooled prismatic-type reactor, the benchmark problem developed by Argonne National Laboratory [32] was solved. Fig. 5.1 illustrates the one-twelfth GCMR core. The design employs a graphite structure with TRISO fuel blocks (19.95 at% UCO fuel) of 40% TRISO packing fraction, YH_2 moderator pins with cladding, helium coolant holes, a Gd_2O_3 burnable poison block, a BeO reflector, and twelve control drums positioned in the reflector surrounding the core. Since SSAPI currently has no capability to handle non-fuel TRISO particles, the Gd_2O_3 burnable poison particles were homogenized with their graphite binder for modeling. Three assembly types are used, and the central assembly can accommodate a B_4C control rod through a guide tube, though no control rods are inserted in this model. The actual benchmark specification was taken from [38], to which the reader is referred for further details.

The Serpent2 simulation used 500 inactive and 2,000 active cycles and 10^6 histories per cycle. For griffin calculation, a sensitivity study indicated that this problem is highly sensitive to angular quadrature due to the large number of burnable poison blocks. To ensure accuracy, both angular and spatial discretizations were applied very tightly. Specifically, seven polar angles and eighteen

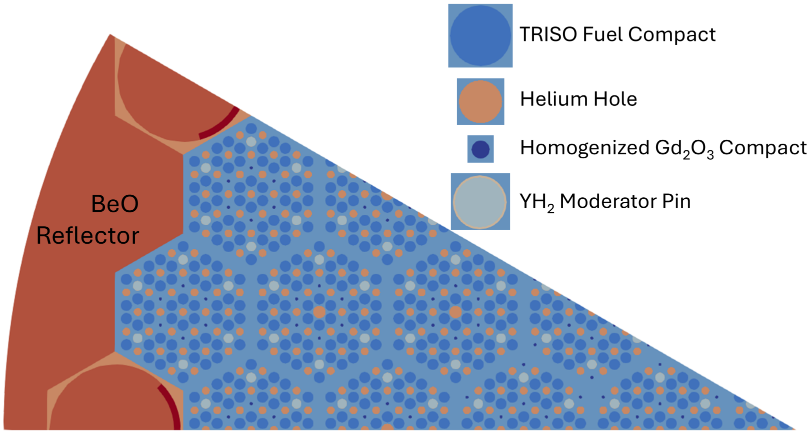

Figure 5.1. One-twelfth GCMR core configuration.

azimuthal angles (504 angles in 2D) were used, together with 113,214 second-order `L2_LAGRANGE` elements. This setup resulted in a total of approximately 34 billion degrees of freedom (DoF)s. For Richardson iteration of the DFEM-SN CMFD solve, the relative tolerance of 10^{-6} was used as the convergence criteria. The simulations were carried out on the INL Bitterroot HPC server using 36 processors.

For SSAPI multigroup library generation, a 7,178-group spectrum was tallied from Serpent2 using a single assembly problem (inner assembly) and subsequently processed in NJOY. It is recommended to use reactor-type- or problem-specific libraries, since no single representative spectrum can adequately cover all advanced reactor designs in only 70 groups. Although an external code was used in this work to obtain the spectrum, Griffin's internal procedure will be extended in the future to automate this process and eliminate the need for external tools.

Table 5.1 summarizes the eigenvalue and pin-power results for the control drum in and out configurations. The reactivity errors of Griffin are -110 and -127 pcm, respectively, indicating that the calculated control drum worth is highly accurate, with only a 0.29% error as shown in Table 5.2. The pin-power distributions also show excellent agreement with the Serpent2 results, remaining within approximately 0.2% root mean square (RMS) error for both configurations. Fig. 5.2 compares the power distributions and corresponding errors for the two configurations, demonstrating that the Griffin solution captures the power-profile shift from the control drum in to out cases very well.

One important observation is that the Griffin results are identical regardless of whether the DCET method or the Tone method is used for Yttrium and Gadolinium resonance treatments. This is encouraging, as the DCET method delivers practically the same solution at only 1% of the computational cost for the Tone method, reducing the total simulation time by about 25%.

Table 5.1. Comparison of Serpent2 and Griffin Results for Control Drum Out/In Cases of GCMR Core

	Control Drum Out				Control Drum In			
	k-eff	$\Delta k/k$ (pcm)	ΔP_{RMS}	ΔP_{MAX}	k-eff	$\Delta k/k$ (pcm)	ΔP_{RMS}	ΔP_{MAX}
Serpent2	1.07686	2 (s.t.d)	0.06% (s.t.d)	0.08% (s.t.d)	1.01231	2 (s.t.d)	0.06% (s.t.d)	0.16% (s.t.d)
Griffin*	1.07559	-110	0.20%	0.56%	1.01101	-127	0.22%	0.75%

* Identical results obtained using the Tone method and the DCET method.

Table 5.2. Comparison of drum worth between Serpent2 and Griffin for GCMR Core

	Drum Worth (%)	Error (%)
Serpent2	5.921	-
Griffin	5.938	0.29

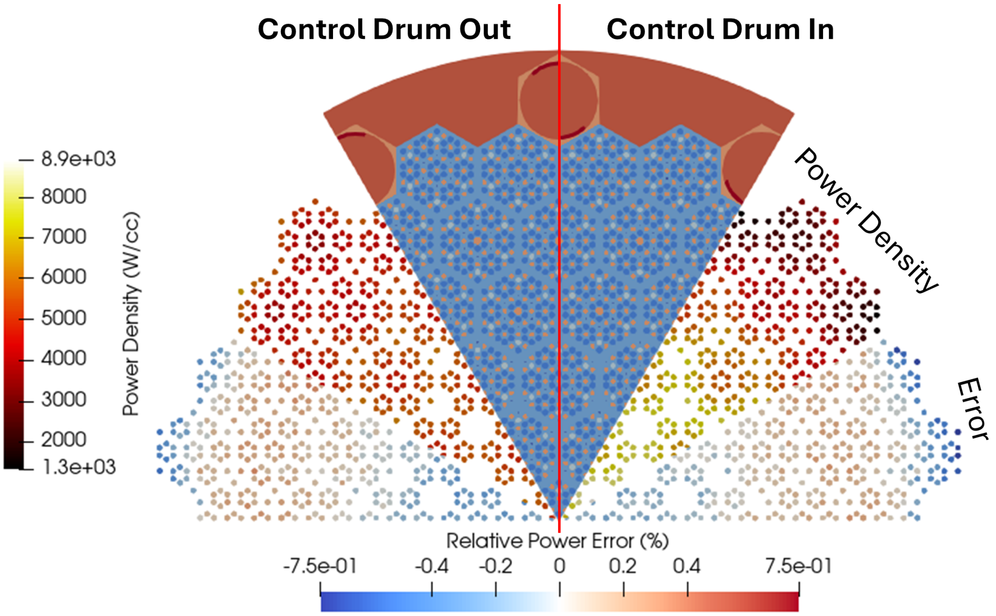

Figure 5.2. Griffin pin power comparison against Serpent2 result for one-twelfth GCMR core.

5.2 HPMR Benchmark

For a heat pipe-cooled prismatic-type reactor, the benchmark problem developed by Argonne National Laboratory [33] was analyzed. Fig. 5.3 illustrates the one-sixth HPMR core, showing both the control drum in and out configurations simultaneously. The core contains a single assembly type, consisting of TRISO compacts with 19.95 at% UCO fuel at a 40% TRISO packing fraction, heat pipes, and YH_2 moderator pins embedded in a graphite block. Its radial dimension is comparable to that of the GCMR core discussed in the previous subsection. The configuration includes 30 fuel assemblies surrounded by a single ring of beryllium reflector and 12 control drums. The dark orange region in Fig. 5.3 represents a homogenized mixture of structural material and air. Further details of the benchmark specification can be found in Reference [39].

The Serpent2 simulation used 250 inactive and 2,000 active cycles and 10^6 histories per cycle. For griffin calculation, three polar angles and six azimuthal angles (72 angles for 2D) were used, together with 88,996 second-order `L2_LAGRANGE` elements. This setup resulted in approximately 3.8 billion total DoFs. For Richardson iteration of the DFEM-SN CMFD solve, the relative tolerance of

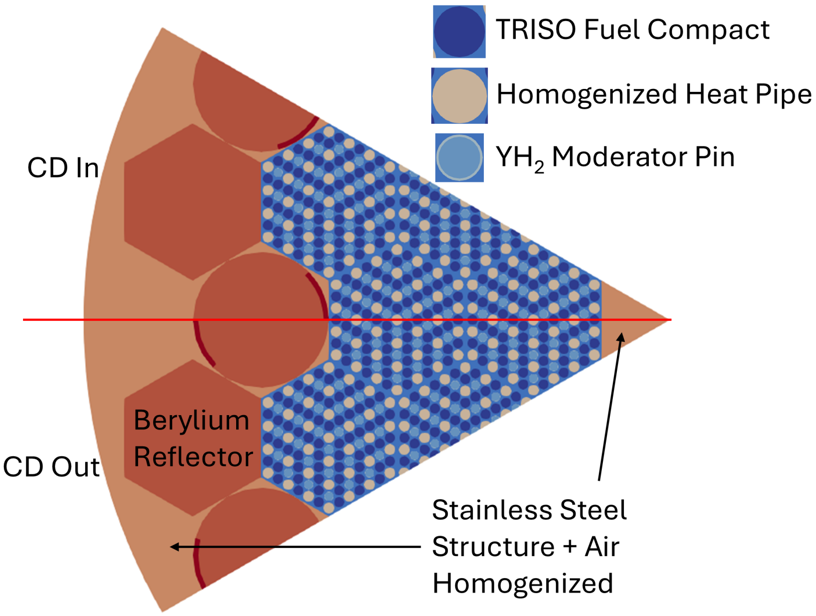

Figure 5.3. One-sixth HPMR core configuration.

10^{-6} was used as the convergence criteria. The simulations were carried out on the INL Bitterroot HPC server using 40 processors.

As in the GCMR case, the SSAPI multigroup library (70-group) was generated using the single-assembly spectrum tallied from Serpent. Table 5.3 summarizes the eigenvalue and pin-power results for the control drum in and out configurations. The reactivity errors of Griffin are 2–38 pcm and 165–187 pcm for control drum out and in configurations, respectively. Although the control drum worth error is slightly larger than in the GCMR case, it still shows good agreement within 1.39%, as presented in Table 5.4. The pin-power distributions also compare well with the Serpent2 results, within 0.36% RMS error for the control drum out case and 0.71% RMS error for the control drum in case. Maximum errors of about 1–2% occur at pins near the beryllium reflectors, while the majority of the pins in the inner core region agree within 1%, as shown in Fig. 5.4.

As in the GCMR case, the DCET method yields results nearly identical to those of the Tone method, differing by only 18 pcm for both configurations and producing almost identical pin-power distributions. For this problem, about 4.5% of the computation time for the Tone method is taken

Table 5.3. Comparison of Serpent2 and Griffin Results for Control Drum Out/In Cases of HPMR Core

	Control Drum Out				Control Drum In			
	k-eff	$\Delta k/k$ (pcm)	ΔP_{RMS}	ΔP_{MAX}	k-eff	$\Delta k/k$ (pcm)	ΔP_{RMS}	ΔP_{MAX}
Serpent2	1.08549	2 pcm (s.t.d)	0.01 % (s.t.d)	0.01 % (s.t.d)	0.97251	2 pcm (s.t.d)	0.01 % (s.t.d)	0.03 % (s.t.d)
Griffin[a]	1.08594	38	0.36 %	0.98 %	0.97428	187	0.71 %	2.24 %
Griffin[b]	1.08551	2	0.35 %	0.96 %	0.97407	165	0.71 %	2.22 %

[a] Results obtained using the DCET method. [b] Results obtained using the Tone method.

Table 5.4. Comparison of drum worth between Serpent2 and Griffin for HPMR Core

	Drum Worth (pcm)	Error (%)
Serpent2	10,703	-
Griffin	10,553	-1.39

for the DCET method, reducing the total simulation time by 30%.

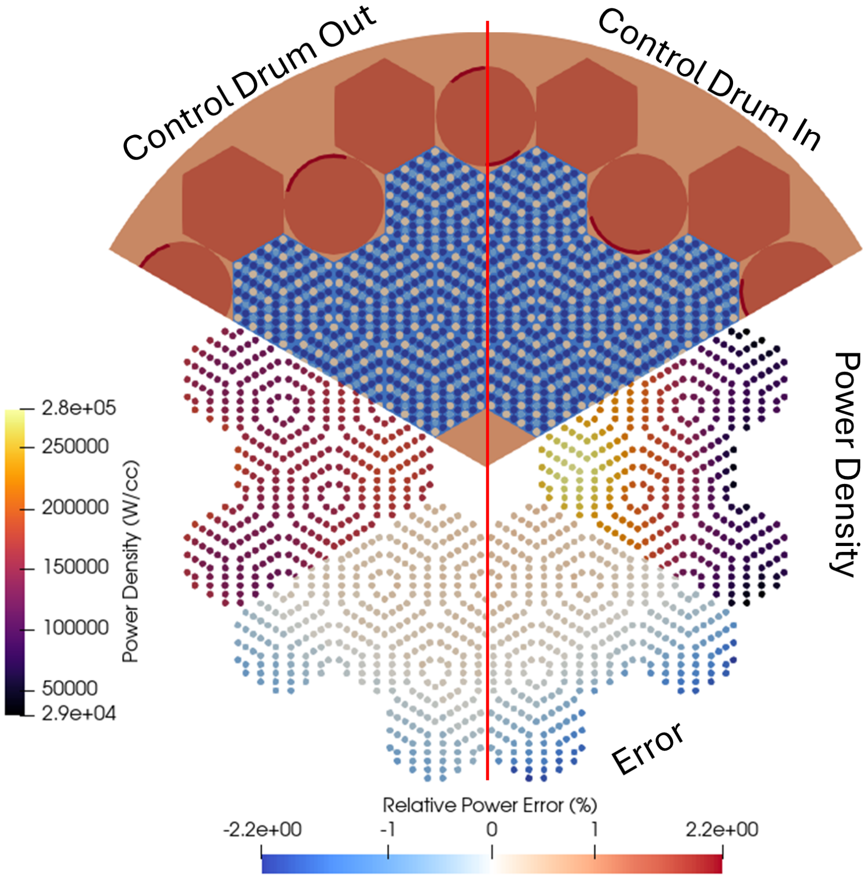

Figure 5.4. Griffin pin power comparison against Serpent2 result for one-sixth HPMR core.

5.3 gPBR Benchmark

For a gas-cooled PBR, a benchmark developed by Idaho National Laboratory [34] was adapted to derive a simplified 2D-RZ model with the same fuel type and pebble configuration. The geometry is shown in Fig. 5.5. The pebble-bed region has a radius of 120 cm and a height of 893 cm, filled with 216,916 pebbles of 3 cm radius, giving a core-average pebble packing fraction of 60.73%. Each pebble consists of a 2.5 cm fuel zone surrounded by a graphite layer, where the fuel zone contains TRISO particles with 15.5 wt.% UCO fuel at a packing fraction of 9.39%.

For the control rods, the original 18 rods were converted to a ring in the RZ geometry, preserving the absorber volume and locating the midpoint of the ring at the original control rod hole center. In the top region above the pebble-bed, the original B_4C number density was preserved. For the

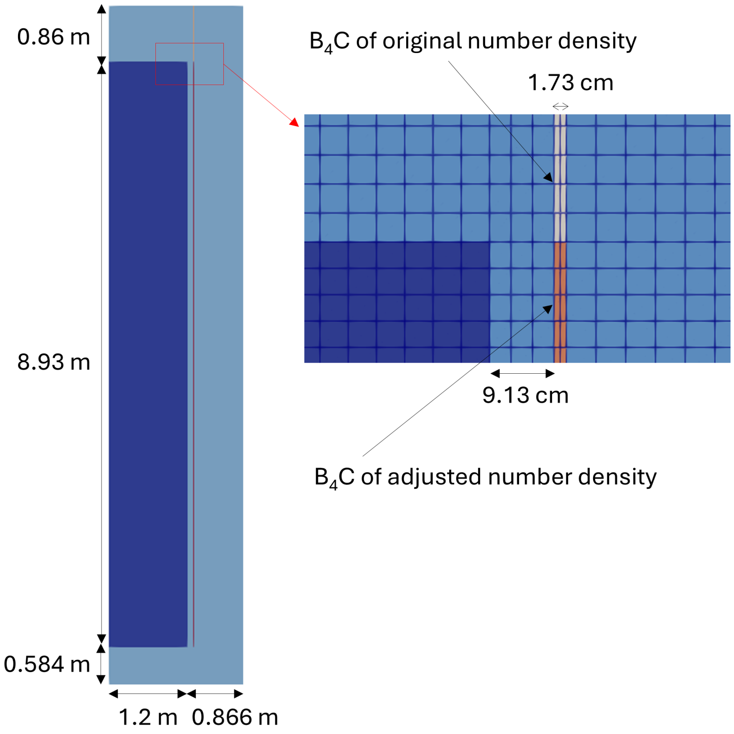

Figure 5.5. gPBR RZ core configuration.

rod-in case, the B_4C number density below the top surface of the pebble-bed was reduced so that the rod worth matches that of the original 3D configuration. Unlike the 3D case, neutrons cannot bypass the absorber in the RZ model, so the number density must be reduced by roughly an order of magnitude.

The Serpent2 simulations used 250 inactive and 1,000 active cycles with 10^6 histories per cycle. Note that a cylindrical control rod is modeled to avoid discrepancies arising from geometry conversion when compared with Griffin models. For Griffin calculations, DFEM-SN transport was performed using three polar and six azimuthal angles (72 total in 2D) and 14,628 first-order `L2_LAGRANGE` elements, as shown in Fig. 5.5. Each square element had a 4 cm side, resulting in approximately 295 million total DoFs. Richardson iteration of the DFEM-SN CMFD solver was used with a relative tolerance of 10^{-6} as the convergence criterion. Simulations were run on the INL Bitterroot HPC server using 72 processors.

Fig. 5.6 shows the XS regions defined to account for spatial variations in pebble volume fraction, as illustrated in Fig. 3.1. Note that pebble locations were generated using a discrete element method (DEM) code, resulting in a larger void fraction in the upper region. A total of 15 XS regions were used. In the periphery, two axial regions of 11.1625 cm height were defined at the top and bottom, and two radial regions of 12 cm width were defined, resulting in a total of $5 \times 3 = 15$ regions. This configuration is motivated by the observation that pebble volume fraction variations tend to approach an asymptotic value beyond approximately four pebble diameters.

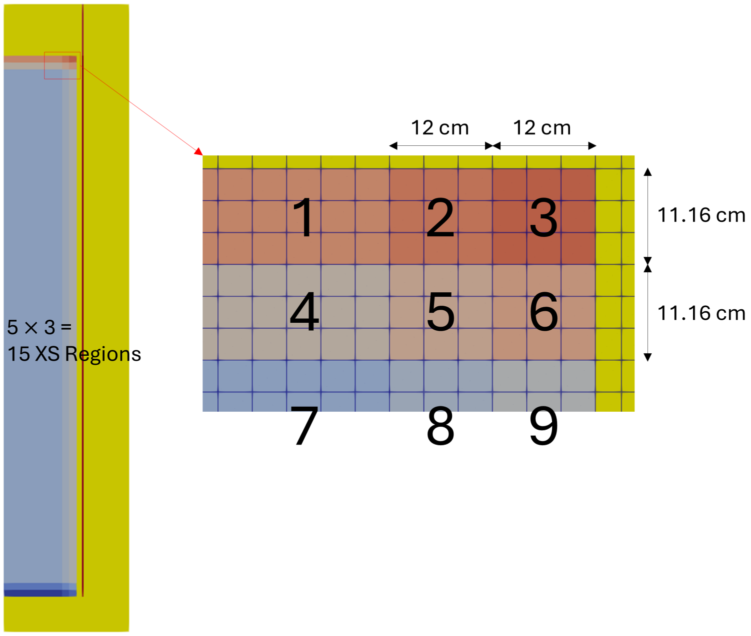

Figure 5.6. XS region setting to account for pebble volume fraction variation. 15 XS regions: 5 axial regions × 3 radial regions.

Table 5.5 summarizes the eigenvalue and pin-power results for the control rod in and out configurations. Three Griffin cases were examined: (a) with streaming correction and using region-wise pebble volume fractions, (b) without streaming correction and using region-wise pebble volume fractions, and (c) with streaming correction and using the core-average pebble volume fraction. Case (a) shows excellent agreement with Serpent, within reactivity errors of 82 pcm and 23 pcm for rod-out and rod-in, respectively, and thus a good prediction of control rod worth (Table 5.6). Case (b) shows large reactivity errors of 263 pcm and 923 pcm, respectively. This is expected, since neglecting streaming correction underestimates leakage, which increases eigenvalue in the rod-out case due to reduced leakage and in the rod-in case due to reduced absorber effectiveness.

Consequently, the control rod worth is underestimated by 9.5%. In case (c), eigenvalues are lower than in (a) because pebbles are uniformly spread throughout the core, reducing the shadowing effect and strengthening resonance absorption in ^{238}U. For the rod-in configuration, the closer proximity of fuel to the control rods further lowers the eigenvalue, resulting in an overestimation of rod worth. The resulting rod worth error is 2.43%, which is acceptable but worse than case (a).

Table 5.5. Comparison of Serpent2 and Griffin Results for Control Rod Out/In Cases of gPBR 2D-RZ Core Problem

	Control Rod Out				Control Rod In			
	k-eff	$\Delta k/k$ (pcm)	ΔP_{RMS}	$\Delta P_{\mathrm{MIN}}/\Delta P_{\mathrm{MAX}}$	k-eff	$\Delta k/k$ (pcm)	ΔP_{RMS}	$\Delta P_{\mathrm{MIN}}/\Delta P_{\mathrm{MAX}}$
Serpent2	1.34935	2 (s.t.d)	0.08 % (s.t.d)	0.24 % (s.t.d)	1.23305	2 (s.t.d)	0.07 % (s.t.d)	0.21 % (s.t.d)
Griffin[a]	1.35084	82	1.31 %	-2.90/3.64 %	1.23340	23	2.00 %	-3.73/5.31 %
Griffin[b]	1.35415	263	2.69 %	-8.55/4.63 %	1.24724	923	3.43 %	-10.01/5.78 %
Griffin[c]	1.34953	10	4.89 %	-4.61/20.03 %	1.23063	-160	6.48 %	-4.75/26.69 %

[a] Results obtained with streaming correction and using region-wise pebble volume fractions.

[b] Results obtained without streaming correction and using region-wise pebble volume fractions.

[c] Results obtained with streaming correction and using core-average pebble volume fraction.

Table 5.6. Comparison of Rod Worth between Serpent2 and Griffin for gPBR 2D-RZ Core Problem

	Rod Worth (pcm)	Error (%)
Serpent2	6,990	-
Griffin w/ Streaming Corr. and Region-wise Pebble Volume Fraction	7,048	0.84
Griffin w/o Streaming Corr. and Region-wise Pebble Volume Fraction	6,330	-9.44
Griffin w/ Streaming Corr. and Core-average Pebble Volume Fraction	7,160	2.43

Fig. 5.7 and Fig. 5.8 show the power distributions and relative errors of the three Griffin cases for the rod-out and rod-in configurations, respectively.

For case (a), the error plots do not exhibit noticeable bias or outliers, but a ∼-2 to ∼+2% top-to-bottom tilt is observed, slightly more pronounced in the rod-in case. This systematic tilt warrants further investigation in the future.

In case (b), the error plots clearly demonstrate the impact of underestimated leakage: higher power appears in the core center and lower power at the periphery, with the rod-in configuration showing a stronger effect. Quantitatively, Table 5.5 indicates that neglecting the streaming effect leads to a power tilt of approximately -5 to -6% at the center and ∼+1% at the periphery.

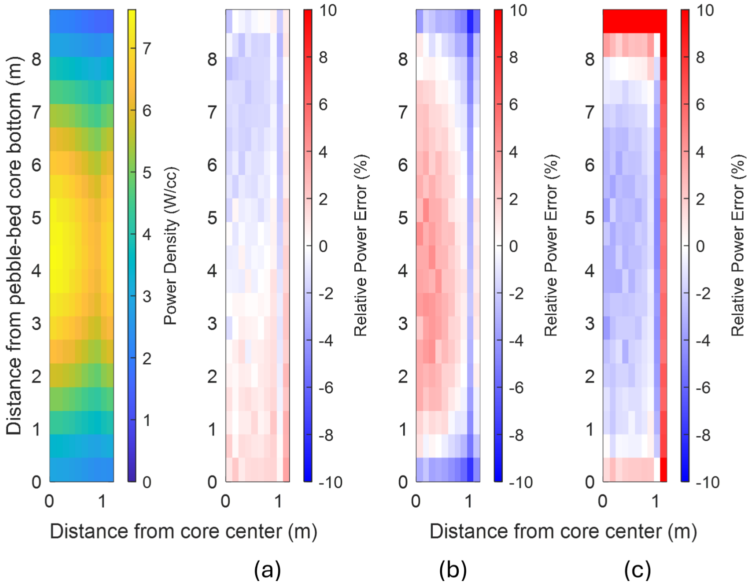

Figure 5.7. gPBR **rod-out** configuration: Griffin power distribution compared to Serpent. Relative errors are shown for (a) streaming correction with region-wise pebble volume fractions, (b) without streaming correction using region-wise fractions, and (c) streaming correction with core-average pebble volume fraction.

Case (c) errors are directly attributable to the use of core-averaged instead of region-wise pebble volume fractions. The difference in packing fractions results in additional +17 to +21% errors at the periphery and -1 to -2% errors at the center, reflecting the magnitude of the pebble volume fraction discrepancy itself.

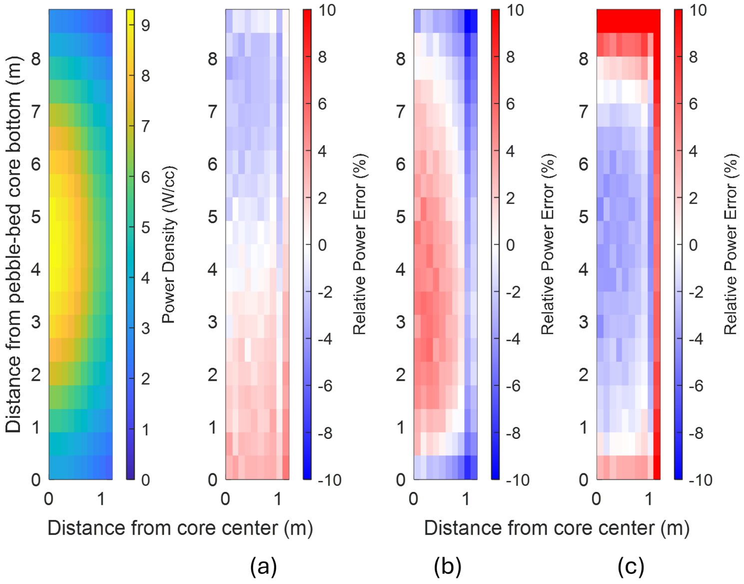

Figure 5.8. gPBR **rod-in** configuration: Griffin power distribution compared to Serpent. Relative errors are shown for (a) streaming correction with region-wise pebble volume fractions, (b) without streaming correction using region-wise fractions, and (c) streaming correction with core-average pebble volume fraction.

5.4 gFHR Benchmark

For PB-FHR, a benchmark developed by Idaho National Laboratory [35] was directly adopted. The geometry is shown in Fig. 5.9. The pebble-bed region has a radius of 120 cm and a height of 309.47 cm, filled with 250,190 pebbles of 2 cm radius, corresponding to a core-average pebble packing fraction of 59.88%. Each pebble consists of a spherical-shell fuel zone with an inner radius of 1.38 cm and an outer radius of 1.8 cm. The region inside the shell is graphite, while a 0.2 cm-thick graphite layer surrounds the outer surface of the shell. The fuel zone contains TRISO particles with 19.55 wt.% UCO fuel at a packing fraction of 22.0%. Beyond the radial graphite reflector, the core barrel, salt downcomer, and reactor pressure vessel are modeled in a simplified manner. The control rods were converted into a cylindrical ring in the same way as in the gPBR case.

The Serpent2 simulations used 250 inactive and 500 active cycles with 10^6 histories per cycle. Similarly to the gPBR benchmark, a cylindrical control rod is modeled to avoid discrepancies arising from geometry conversion when compared with Griffin models. For Griffin calculations,

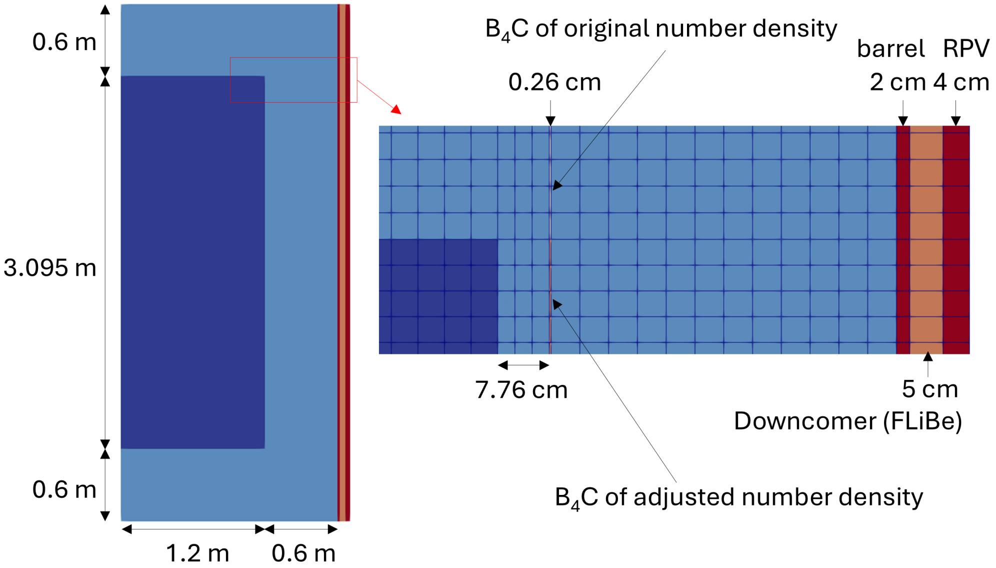

Figure 5.9. gFHR RZ core configuration.

DFEM-SN transport was performed using three polar and six azimuthal angles (72 total in 2D) and 14,628 first-order `L2_LAGRANGE` elements, as shown in Fig. 5.5. Each square element had a 4 cm side, resulting in approximately 295 million total DoFs. Richardson iteration of the DFEM-SN CMFD solver was used with a relative tolerance of 10^{-6} as the convergence criterion. For gFHR, an additional diffusion calculation was performed because the control rod hole contains no void region, but the salt coolant. For this diffusion calculation, a finer mesh was employed by setting "uniform_refine=1" in the mesh block. Simulations were run on the INL Bitterroot HPC server using 72 processors.

The XS region partitioning matches the gPBR case, with 15 regions (5×3). The only difference is the axial thickness of the top and bottom XS layers: 3.87 cm instead of 11.16 cm. For this gFHR model, however, the Serpent2 2 disperse function was used instead of a DEM code, yielding a more uniform pebble distribution up to the top surface of the pebble-bed region, as shown in Fig. 5.10. Compared with Fig. 3.1, deviations of the local pebble volume fraction from the core-averaged value are substantially smaller in this case.

The XS region setting was done as in the gPBR case: 15 regions ($=5\times3$). The only difference is the axial length of the two top and bottom layers of XS regions: 3.87 cm instead of 11.16 cm. For this gFHR problem, however, the disperse function of Serpent2 code was used instead of a DEM code, thus pebbles are more uniformly distributed up to the top surface of the pebbleb-bed region as illustrated in Fig. 5.10. Compared to Fig. 3.1, variations of pebble volume fractions to the core averaged value are much weaker for this problem.

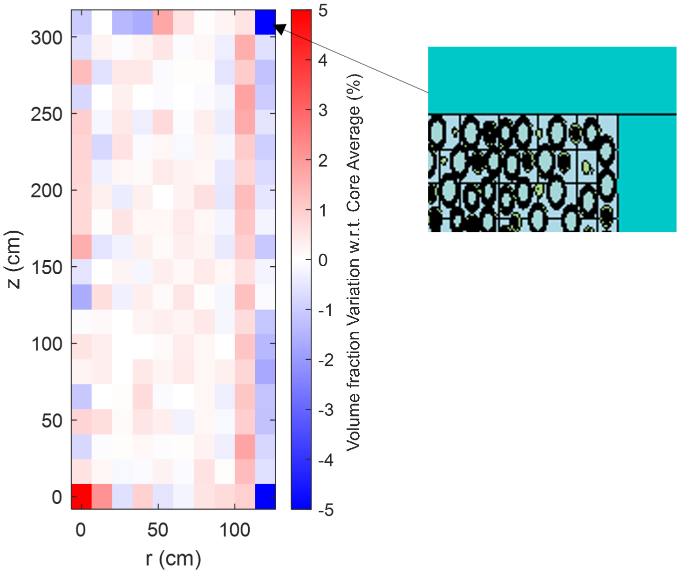

Figure 5.10. Variations of local pebble volume fractions relative to the core average used for gFHR problem.

Table 5.7 summarizes the eigenvalue and pin-power results for the rod-in and rod-out configurations. For Griffin, both transport and diffusion calculations were performed. In both cases, region-wise pebble volume fractions and Benoist–based homogenization were applied. Using core-averaged pebble volume fractions or conventional homogenization did not significantly change the results. The calculations show good agreement, with reactivity errors of 103 pcm (rod-out) and 127 pcm (rod-in) for transport, and 96 pcm (rod-out) and 75 pcm (rod-in) for diffusion; consequently, the predicted control-rod worth (Table 5.8) is within about ±1%. Rod worth from diffusion is higher because the diffusion approximation overestimates leakage, increasing control-rod absorption relative to transport.

Fig. 5.11 and Fig. 5.12 show the power distributions and relative-error maps from the transport and diffusion calculations for the rod-out and rod-in configurations, respectively. The advantage of transport is evident in the power distributions: diffusion exhibits a slight axial power tilt, whereas

Table 5.7. Comparison of Serpent2 and Griffin Results for Control Rod Out/In Cases of gFHR 2D-RZ Core Problem

	Control Rod Out				Control Rod In			
	k-eff	$\Delta k/k$ (pcm)	ΔP_{RMS}	$\Delta P_{\mathrm{MIN}}/\Delta P_{\mathrm{MAX}}$	k-eff	$\Delta k/k$ (pcm)	ΔP_{RMS}	$\Delta P_{\mathrm{MIN}}/\Delta P_{\mathrm{MAX}}$
Serpent2	1.32679	3 (s.t.d)	0.1 % (s.t.d)	0.24 % (s.t.d)	1.28721	3 (s.t.d)	0.09 % (s.t.d)	0.21 % (s.t.d)
Griffin[a]	1.32860	103	0.83 %	-5.17/2.26 %	1.28931	127	0.81 %	-4.97/1.98 %
Griffin[b]	1.32848	96	1.51 %	-8.39/2.66 %	1.28846	75	1.22 %	-6.71/2.62 %

[a] Transport results, [b] Diffusion results

Table 5.8. Comparison of Rod Worth between Serpent2 and Griffin for gFHR 2D-RZ Core Problem

	Rod Worth (pcm)	Error (%)
Serpent2	2,318	-
Griffin Transport	2,294	-1.02
Griffin Diffusion	2,338	0.90

transport does not. Consequently, the RMS power-distribution error is below 1% for transport and about 1.2–1.5% for diffusion. The tilt appears to be related to the strong absorber above the pebble-bed region, where the absorber density was not adjusted in the RZ transformation. In a full 3D configuration, this effect is expected to be weaker, but its impact should be assessed in a realistic 3D model. Note that the transport calculation can explicitly resolve this strong-absorber effect. This analysis also suggests a possible explanation for the slight power tilt observed even in the transport solution for the gPBR problem (panel (a) of Fig. 5.7 and Fig. 5.8): insufficient angular quadrature; a detailed investigation is left for future work.

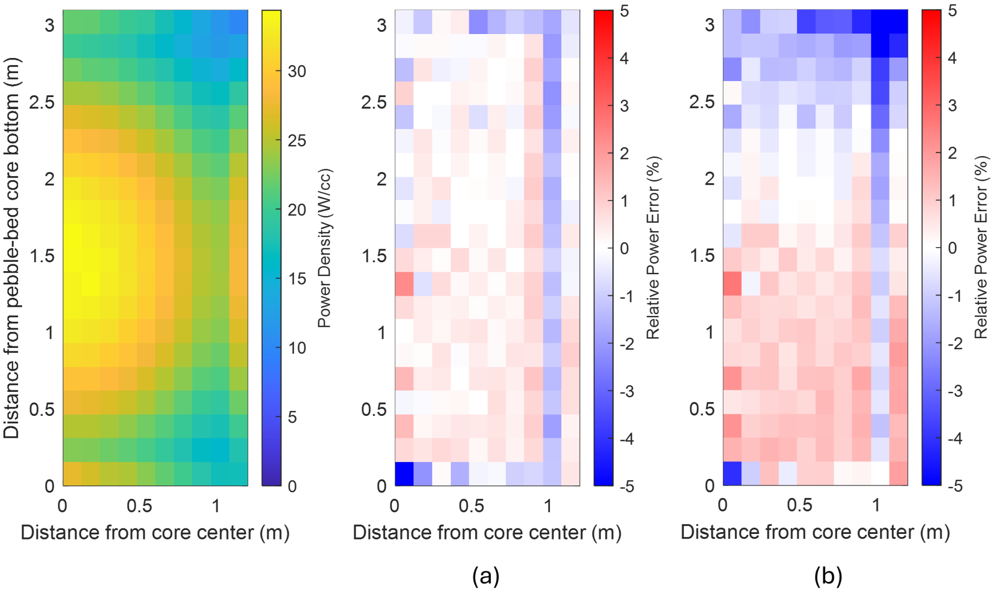

(a)

(b)

Figure 5.11. gFHR **rod-out** configuration: Griffin power distribution compared to Serpent. Relative errors are shown for (a) transport and (b) diffusion.

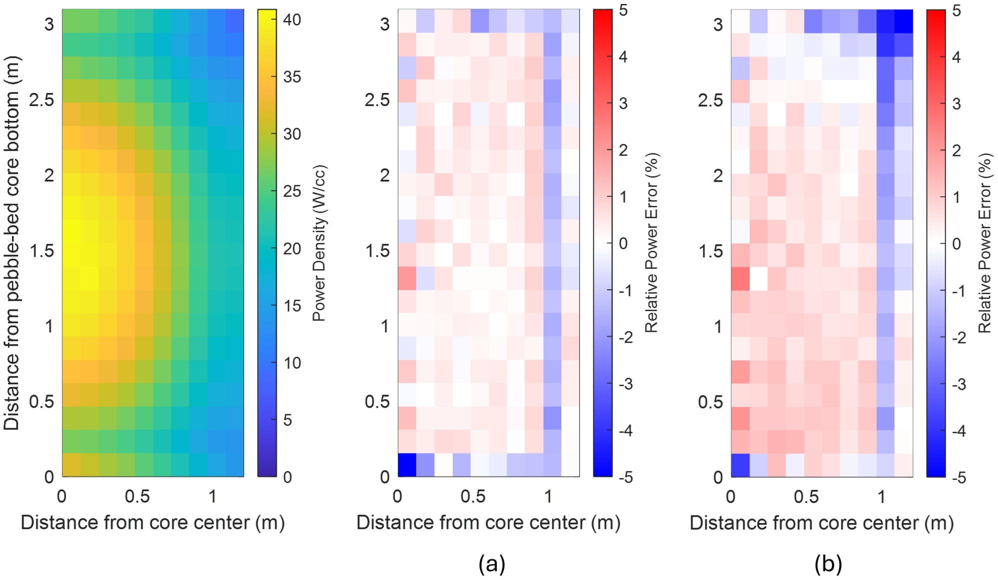

(a)

(b)

Figure 5.12. gFHR **rod-in** configuration: Griffin power distribution compared to Serpent. Relative errors are shown for (a) transport and (b) diffusion.

6. Conclusions and Future Work

The recent development of Griffin's online multigroup XS generation capability (SSAPI) has focused on improving accuracy and performance for both prismatic and pebble-bed reactor applications. Key advancements for both types of reactors include an improved unit-cell-based slowing-down method applicable to both TRISO particle (micro-level) and compact or pebble (macro-level) self-shielding in a unified framework; an extension of the methodology to annular compact typical of HTGR designs and spherical shell fuel zones typical of PB-FHR designs; and an initial demonstration of on-the-fly group condensation with consistent P0 transport correction.

For prismatic reactors, specific improvements include enhanced treatments for non-fuel resonance treatment and a multigroup equivalence correction method to mitigate ultrafine-group-to-fine-group condensation errors. For gas-cooled pebble-bed reactors, a streaming correction technique was implemented to account for the strong streaming effects arising from void regions between pebbles. In addition, verification tests revealed that accounting for local pebble volume fraction variations is essential for capturing correct pebble-to-pebble shadowing effects and achieving accurate local power distributions. Together, these improvements significantly enhance the accuracy, robustness, and performance of self-shielding calculations.

The significance of each advancement is briefly summarized as follows.

1. **Improved slowing down method for fuel self-shielding**

   The previous two-stage TRISO self-shielding treatment has been replaced with a more robust and faster method in a unified framework for both TRISO-cell and macro-cell problems. The new approach directly applies the Dancoff correction to CP coefficients using a bell function, eliminating the need to derive equivalent 1D cells. The former method sometimes failed during the search for equivalent cells, whereas the new method avoids such failures entirely, saving computational effort and increasing robustness. The total computational time for the self-shielding treatment of a fuel pin containing TRISO is now on the order of 0.5 seconds, which represents an unprecedented level of performance. For example, the fuel self-shielding treatment for the full HPMR 2D core takes roughly $\sim$20 seconds using 40 processors or $\sim$40 seconds using 20 processors in an HPC environment.

2. **Improved treatment for non-fuel self-shielding**

   Non-fuel self-shielding can be treated either with the Tone method, which is applicable to arbitrary unstructured geometries, or with an advanced Equivalence Theory improved using the bell function concept for geometries that can be represented by a pin structure. The homogeneous RI table was improved and made compatible with the Tone method, eliminating the need for users to prepare separate heterogeneous tables for their target problems. The latter method, named Dancoff Category-based Equivalence Theory (DCET), provides results that are nearly identical to those of the Tone method, but at only a fraction of the computational cost, since it requires solving far fewer fixed-source problems. As a result, the non-fuel resonance treatment cost is reduced by several orders of magnitude, leading to an overall reduction in total simulation time by approximately 20–25%. With these improvements, the combined cost of fuel and non-fuel resonance self-shielding now accounts for less than 3% of the total simulation time (and in some cases, even less than 1%).

3. **On-the-fly multigroup equivalence**

   For problems with high fuel density compacts surrounded by significant moderator, neglecting the angular dependence of resonance multigroup XSs can introduce a non-negligible negative reactivity bias of up to –300 to –400 pcm. To ensure accuracy across a broad range of reactor configurations, a multigroup equivalence parameter, the SPH factor, is calculated on-the-fly and applied to the fuel regions. This approach effectively mitigates the bias and recovers most of the error observed without the correction.

4. **Advanced pebble-bed homogenization method**

   Homogenization is performed using a multi-pebble model that accounts for distinct flux weighting among different pebble types, which is particularly important when fresh and burned pebbles are mixed. For gas-cooled PBRs, the strong streaming effect is captured using the Benoist method in both diffusion and transport calculations. Verification tests demonstrated that neglecting the streaming effect can lead to significant errors: –5 to –6% in power at the core center, +1% at the periphery, eigenvalue overestimations of +200 pcm (rod-out) and +900 pcm (rod-in), and –10% in control rod worth. Incorporating the correction successfully mitigated these errors.

5. **Local pebble volume fraction calculation**

   Using a core-average pebble volume fraction underestimates the pebble-to-pebble shadowing effect, leading to stronger ^{238}U resonance absorption and a negative reactivity bias. Closer fuel proximity to the control rods further amplifies this bias, resulting in an additional positive bias in the control rod worth. Local power errors can reach several tens of percent. To address this, a test script for performing axial integration of circle–sphere intersection areas was developed and verified. The algorithm executes essentially instantaneously, making it practical for integration into routine calculations.

As an additional effort to reduce computational cost, a proof-of-concept demonstration of on-the-fly condensation from fine-group to broad-group structures was carried out using the consistent P_0 transport correction. The method iterates between fine-group fixed source solves and broad-group eigenvalue solves, yielding solutions very close to direct fine-group calculations: eigenvalue within 10 pcm and pin power within 0.5%. Observations indicate that around eight or fewer broad groups are sufficient for the tested problems including the 2D HPMR core. Although little performance gain was realized so far due to the current unaccelerated source-iteration fixed source solver, significant improvements are expected once a GMRES solve with DSA preconditioning is implemented.

Verification tests have been carried out for advanced reactor types of current interest, including GCMR, HPMR, gas-cooled PBR, and salt-cooled FHR. In all cases, Griffin demonstrates excellent agreement with Serpent2 in eigenvalue, pin power distribution, and control rod or drum worth, confirming the accuracy and robustness of the developed methodologies. The error of each case are summarized below:

- GCMR: –110 to –127 pcm reactivity, 0.2% RMS pin power, 0.29% control drum worth
- HPMR: 38 to 187 pcm reactivity, 0.36 to 0.71% RMS pin power, –1.39% control drum worth
- gPBR: 23 to 82 pcm reactivity, 1.31 to 2.0% RMS local power, 0.84% control rod worth
- gFHR: 103 to 127 pcm reactivity, 0.8% RMS local power, –1% control rod worth

It should also be emphasized that XS generation accounts for less than 3% of the total simulation time across all four benchmark test cases.

To conclude, Griffin's online cross section generation capability has demonstrated strong performance for a wide range of TRISO-fueled reactor problems. Although not explicitly analyzed here, it also supports pebble-bed depletion calculations [4]. Future work will focus on the following:

- Performance improvements to the fine-group fixed-source solver for on-the-fly condensation
- Extension of depletion capabilities to prismatic-type reactor problems
- Transient analysis for single- and multi-physics calculations
- Support for coupled neutron–gamma transport calculations
- Applications to thermal molten-salt reactors
- Streamlined library generation procedure accounting for problem-specific spectrum
- Extension of double-heterogeneity treatment to non-fuel particles
- Extended verification and validation activities

Once this planned future work is carried out, Griffin will become a powerful reactor physics tool, fully capable of generating its own XS without external support, and will play a central role in advanced reactor design and analysis.

REFERENCES

[1] Y. Wang, Z. M. Prince, H. Park, O. W. Calvin, N. Choi, Y. S. Jung, S. Schunert, S. Kumar, J. T. Hanophy, V. M. Labouré, C. H. Lee, J. Ortensi, L. H. Harbour, and J. R. Harter, “Griffin: A MOOSE-based reactor physics application for multiphysics simulation of advanced nuclear reactors,” *Ann. Nucl. Energy*, vol. 211, 110917, 2025.

[2] C. H. Lee and J. Ortensi, et al., “Griffin Software Development Plan,” Research Report ANL/NSE-21/23, INL/EXT-21-63185, Argonne National Laboratory, Idaho National Laboratory, June 2021.

[3] H. Park, C. Lee, Y. S. Jung, Y. Wang, O. Calvin, and J. Ortensi, “Cross section generation capability in Griffin,” Tech. Rep. ANL/NSE-21/65 and INL/EXT-21-64567, Argonne National Laboratory and Idaho National Laboratory, 2021.

[4] J. Hanophy, H. Park, V. Laboure, Y. S. Jung, S. Schunert, Y. Wang, and J. Ortensi, “Initial demonstration of new Griffin technologies for simulating the running-in phase of pebble-bed reactors,” Tech. Rep. INL/RPT-23-03821, ANL/NSE-23/61, Idaho National Laboratory and Argonne National Laboratory, 2023.

[5] Y. S. Jung, N. Choi, H. Park, S. Kumar, Y. Wang, and C. H. Lee, “Performance improvements of the Griffin solvers in FY24,” Tech. Rep. ANL/NSE-24/71, INL/RPT-24-80851, Argonne National Laboratory and Idaho National Laboratory, 2024.

[6] S. Choi, C. H. Lee, and D. Lee, “Resonance treatment using pin-based pointwise energy slowing-down method,” *J. Comput. Phys.*, vol. 330, pp. 134–155, 2017.

[7] H. S. Park, W. S. Yang, and C. H. Lee, “Particulate fuel modeling of MC^2-3 using iterative local spatial self-shielding method,” *Ann. Nucl. Energy*, vol. 172, p. 109060, 2022.

[8] C. H. Lee and Y. S. Jung, “Verification of the cross section library generated using OpenMC and MC^2-3 for PROTEUS,” *PHYSOR 2018*, Cancun, Mexico, April 2018.

[9] H. Park and H. G. Joo, “Practical resolution of angle dependency of multigroup resonance cross sections using parametrized spectral superhomogenization factors,” *Nucl. Eng. Technol.*, vol. 49, pp. 1287–1300, 2017.

[10] H. Park, Y. S. Jung, C. H. Lee, Y. Wang, and J. Ortensi, “Initial assessment of online cross section generation capability of Griffin for gas-cooled pebble-bed reactor,” in *PHYSOR 2024*, April San Francisco, CA, 2024.

[11] P. Benoist, “Streaming effects and collision probabilities in lattices,” *Nucl. Sci. Eng.*, vol. 34, pp. 285–307, 1968.

[12] H. Park, Y. S. Jung, and C. H. Lee, “Bell function-based analytic two-region slowing down method for double heterogeneous problem,” in *American Nuclear Society Transactions, ANS Winter Meeting*, November Orlando, FL, 2024.

[13] W. Ji, C. Liang, and N. E. Pusateri, “Analytical Dancoff factor evaluations for reactor designs loaded with TRISO particle fuel,” *Ann. Nucl. Energy*, vol. 63, pp. 665–673, 2014.

[14] W. Ji and R. W. Martin, “Application of the chord method to obtain analytical expressions for Dancoff factors in stochastic media,” *Nucl. Sci. Eng.*, vol. 169, pp. 19–39, 2011.

[15] A. Talamo, “Analytical calculation of the average Dancoff factor for prismatic high-temperature reactors,” *Nucl. Sci. Eng.*, vol. 156, pp. 343–356, 2007.

[16] S. Choi, H. Lee, S. G. Hong, and D. Lee, “Resonance self-shielding methodology of new neutron transport code STREAM,” *J. Nucl. Sci. Technol.*, vol. 52, pp. 1133–1150, 2015.

[17] H. Koike, K. Yamaji, K. Kirimura, D. Sato, H. Matsumoto, and A. Yamamoto, “Advanced resonance self-shielding method for gray resonance treatment in lattice physics code GALAXY,” *J. Nucl. Sci. Technol.*, vol. 49, pp. 725–747, 2012.

[18] A. J. Janssen, “Enkele opmerkingen over de Dancoff factor,” Tech. Rep. FYS-LWR-89-11, Netherlands Energy Research Foundation, 1990.

[19] N. Sugimura and A. Yamamoto, “Resonance treatment based on ultra-fine-group spectrum-calculation in the AEGIS code,” *J. Nucl. Sci. Technol.*, vol. 44, pp. 958–966, 2007.

[20] A. Hébert, “Advances in the development of a subgroup method for the self-shielding of resonant isotopes in arbitrary geometries,” *Nucl. Sci. Eng.*, vol. 126, pp. 245–263, 1997.

[21] Y. Liu and W. R. Martin, “Assessment of homogeneous and heterogeneous resonance integral tables and their applications to the embedded self-shielding method,” *Ann. Nucl. Energy*, vol. 92, pp. 186–197, 2016.

[22] H. Park, *Resonance Treatment Innovations for Efficiency and Accuracy Enhancement in Direct Whole Core Calculations of Water-Cooled Power Reactors*. PhD thesis, Seoul National University, 2018.

[23] M. L. Williams and K.-S. Kim, “The embedded self-shielding method,” in *PHYSOR 2012 – Advances in Reactor Physics – Linking Research, Industry, and Education*, American Nuclear Society, 2012-04.

[24] A. Hébert and R. Chambon, “A PyNJOY-2012 tutorial,” Tech. Rep. IGE–361, Institut de g´enie nucl´eaire D´epartement de g´enie m´ecanique Ecole Polytechnique de Montr´eal, 2012.

[25] T. Tone, “A numerical study of heterogeneity effects in fast reactor critical assemblies,” *J. Nucl. Sci. Technol.*, vol. 12, pp. 467–481, 2012.

[26] S. Schunert, J. Ortensi, Y. Wang, P. Balestra, M. Jaradat, O. Calvin, J. Hanophy, and L. Harbour, “An equilibrium core depletion algorithm for pebble-bed reactors in the Griffin code,” *Ann. Nucl. Energy*, vol. 192, p. 109980, 2023.

[27] E. Teuchert, U. Hansen, and K. A. Haas, “VSOP - computer code system for reactor physics and fuel cycle simulation,” Tech. Rep. JUEL–1649, Kernforschungsanlage Juelich G.m.b.H. (Germany, F.R.). Inst. fuer Reaktorentwicklung, 1980.

[28] J. Lieberoth and A. Stojadinović, “Neutron streaming in pebble beds,” *Nucl. Sci. Eng.*, vol. 76, pp. 336–344, 1980.

[29] S. Douglass and F. Rahnema, “Subgroup decomposition method,” *Ann. Nucl. Energy*, vol. 48, pp. 84–101, 2012.

[30] G. I. Bell, G. E. Hansen, and H. A. Sandmeier, “Multitable treatments of anisotropic scattering in S_N multigroup transport calculation,” *Nucl. Sci. Eng.*, vol. 28, pp. 376–383, 1967.

[31] IAEA, “WIMS-D library update,” Tech. Rep. ISBN 92–0–105006–2, IAEA, 2007.

[32] A. Abdelhameed, Y. Cao, D. Nunez, Y. Miao, K. Mo, C. H. Lee, E. Shemon, and N. E. Stauff, “High-fidelity multiphysics modeling of load following for 3-D gas-cooled microreactor assembly using NEAMS codes,” *Transactions of the American Nuclear Society*, vol. 127, pp. 994–997, 2022.

[33] N. E. Stauff, K. Mo, Y. Cao, J. W. Thomas, Y. Miao, C. H. Lee, C. Matthews, and B. Feng, “Preliminary applications of neams codes for multiphysics modeling of a heat pipe microreactor,” *Transactions of the American Nuclear Society*, vol. 124, pp. 21–24, 2021.

[34] R. Stewart, D. Reger, and P. Balestra, “Demonstrate capability of neamstools to generate reactor kinetics parameters for pebble-bed HTGRs transient modeling,” Tech. Rep. INL/EXT-21-64176, Idaho National Laboratory, 2021.

[35] J. Ortensi, C. M. Mueller, S. Terlizzi1, G. Giudicelli, and S. Schunert, “Fluoride-cooled high temperature pebble-bed reactor reference plant model,” Tech. Rep. INL/RPT-23-72727, Idaho National Laboratory, 2023.

[36] J. Leppänen, “Serpent – a continuous-energy Monte Carlo reactor physics burnup calculation code,” tech. rep., VTT Technical Research Centre of Finland, 2015.

[37] R. E. MacFarlane, D. W. Muir, R. M. Boicourt, and A. C. Kahler, “The NJOY nuclear data processing system, version 2012,” Tech. Rep. LA-UR-12-27079, Los Alamos National Laboratory, 2012.

[38] A. Abdelhameed, Y. Miao, and N. Stauff, “Neutronic modeling of the whole core gas-cooled microreactor (GCMR).” `https://mooseframework.inl.gov/virtual_test_bed/microreactors/gcmr/GCMR_Core_Neutronics.html`. Accessed: 2025-09-30.

[39] N. Stauff, “Heat-pipe micro reactor (MR) description.” `https://mooseframework.inl.gov/virtual_test_bed/microreactors/mrad/reactor_description.html`. Accessed: 2025-09-30.

Nuclear Science and Engineering Division

Argonne National Laboratory
9700 South Cass Avenue, Bldg. 208
Argonne, IL 60439-4842

`www.anl.gov`